

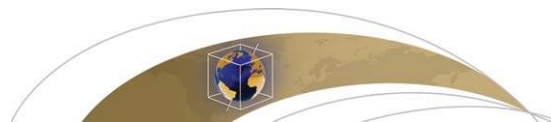


# Open Access Articles

## ***Ages and magnetic structures of the South China Sea constrained by deep tow magnetic surveys and IODP Expedition 349***

The Faculty of Oregon State University has made this article openly available.  
Please share how this access benefits you. Your story matters.

<b>Citation</b>	Li, C.-F., et al. (2014). Ages and magnetic structures of the South China Sea constrained by deep tow magnetic surveys and IODP Expedition 349. <i>Geochemistry Geophysics Geosystems</i> , 15(12), 4958–4983. doi:10.1002/2014GC005567
<b>DOI</b>	10.1002/2014GC005567
<b>Publisher</b>	American Geophysical Union
<b>Version</b>	Version of Record
<b>Terms of Use</b>	<a href="http://cdss.library.oregonstate.edu/sa-termsofuse">http://cdss.library.oregonstate.edu/sa-termsofuse</a>



# Geochemistry, Geophysics, Geosystems

## RESEARCH ARTICLE

10.1002/2014GC005567

### Key Points:

- Deep tow magnetics and IODP Expedition 349 constrained opening history
- Variations are observed in spreading rate and onset of drifting and ridge jump
- Magnetic anomalies are not primarily sourced from the top 100 m of the basement

### Correspondence to:

C.-F. Li,  
cfl@tongji.edu.cn

### Citation:

Li, C.-F., et al. (2014), Ages and magnetic structures of the South China Sea constrained by deep tow magnetic surveys and IODP Expedition 349, *Geochem. Geophys. Geosyst.*, 15, 4958–4983, doi:10.1002/2014GC005567.

Received 5 SEP 2014

Accepted 25 NOV 2014

Accepted article online 4 DEC 2014

Published online 27 DEC 2014

## Ages and magnetic structures of the South China Sea constrained by deep tow magnetic surveys and IODP Expedition 349

Chun-Feng Li<sup>1</sup>, Xing Xu<sup>2</sup>, Jian Lin<sup>3</sup>, Zhen Sun<sup>4</sup>, Jian Zhu<sup>3</sup>, Yongjian Yao<sup>2</sup>, Xixi Zhao<sup>1</sup>, Qingsong Liu<sup>5</sup>, Denise K. Kulhanek<sup>6</sup>, Jian Wang<sup>1</sup>, Taoran Song<sup>1</sup>, Junfeng Zhao<sup>4</sup>, Ning Qiu<sup>4</sup>, Yongxian Guan<sup>2</sup>, Zhiyuan Zhou<sup>1</sup>, Trevor Williams<sup>7</sup>, Rui Bao<sup>8</sup>, Anne Briais<sup>9</sup>, Elizabeth A. Brown<sup>10</sup>, Yifeng Chen<sup>11</sup>, Peter D. Clift<sup>12</sup>, Frederick S. Colwell<sup>13</sup>, Kelsie A. Dadd<sup>14</sup>, Weiwei Ding<sup>15</sup>, Iván Hernández Almeida<sup>16</sup>, Xiao-Long Huang<sup>17</sup>, Sangmin Hyun<sup>18</sup>, Tao Jiang<sup>19</sup>, Anthony A. P. Koppers<sup>13</sup>, Qianyu Li<sup>20</sup>, Chuanlian Liu<sup>20</sup>, Zhifei Liu<sup>1</sup>, Renata H. Nagai<sup>21</sup>, Alyssa Peleo-Alampay<sup>22</sup>, Xin Su<sup>23</sup>, Maria Luisa G. Tejada<sup>24</sup>, Hai Son Trinh<sup>25</sup>, Yi-Ching Yeh<sup>26</sup>, Chuanlun Zhang<sup>20</sup>, Fan Zhang<sup>3</sup>, and Guo-Liang Zhang<sup>27</sup>

<sup>1</sup>State Key Laboratory of Marine Geology, Tongji University, Shanghai, China, <sup>2</sup>Guangzhou Marine Geological Survey, Guangzhou, China, <sup>3</sup>Department of Geology and Geophysics, Woods Hole Oceanographic Institution, Woods Hole, Massachusetts, USA, <sup>4</sup>South China Sea Institute of Oceanology, CAS, Guangzhou, China, <sup>5</sup>State Key Laboratory of Lithospheric Evolution, Institute of Geology and Geophysics, CAS, Beijing, China, <sup>6</sup>International Ocean Discovery Program, Texas A&M University, College Station, Texas, USA, <sup>7</sup>Lamont-Doherty Earth Observatory, Columbia University, Palisades, New York, USA, <sup>8</sup>Geologisches Institut, Swiss Federal Institute of Technology, Zürich, Switzerland, <sup>9</sup>Géosciences Environnement Toulouse, Centre National de la Recherche Scientifique, University of Toulouse, Toulouse, France, <sup>10</sup>College of Marine Science, University of South Florida, St. Petersburg, Florida, USA, <sup>11</sup>Key Laboratory of Marginal Sea Geology, Guangzhou Institute of Geochemistry, Chinese Academy of Sciences, Guangzhou, China, <sup>12</sup>Department of Geology and Geophysics, Louisiana State University, Baton Rouge, Louisiana, USA, <sup>13</sup>College of Earth, Ocean and Atmospheric Sciences, Oregon State University, Corvallis, Oregon, USA, <sup>14</sup>Department of Earth and Planetary Sciences, Macquarie University, Sydney, New South Wales, Australia, <sup>15</sup>Key Laboratory of Submarine Geoscience, Second Institute of Oceanography, State Oceanic Administration, Hangzhou, China, <sup>16</sup>Institute of Geography/Oeschger Centre for Climate Change Research, University of Bern, Bern, Switzerland, <sup>17</sup>State Key Laboratory of Isotope Geochemistry, Guangzhou Institute of Geochemistry, Chinese Academy of Sciences, Guangzhou, China, <sup>18</sup>Marine Geology and Geophysics Division, Korea Institute of Ocean Science and Technology, Ansan, South Korea, <sup>19</sup>Department of Marine Science and Engineering, Faculty of Earth Resources, China University of Geosciences, Wuhan, People's Republic of China, <sup>20</sup>School of Ocean and Earth Sciences, Tongji University, Shanghai, China, <sup>21</sup>Department of Physical, Chemical and Geological Oceanography, Universidade de São Paulo, São Paulo-SP, Brazil, <sup>22</sup>National Institute of Geological Sciences, University of the Philippines, Quezon City, Philippines, <sup>23</sup>School of Marine Geosciences, China University of Geosciences, Beijing, China, <sup>24</sup>Japan Agency for Marine-Earth Science and Technology, Kanagawa, Japan, <sup>25</sup>Department of Science and Technology, Ministry of Natural Resources and Environment, Hanoi, Vietnam, <sup>26</sup>Taiwan Ocean Research Institute, Kaohsiung, Republic of China, <sup>27</sup>Key Laboratory of Marine Geology and Environment, Institute of Oceanology, Chinese Academy of Sciences, Qingdao, China

**Abstract** Combined analyses of deep tow magnetic anomalies and International Ocean Discovery Program Expedition 349 cores show that initial seafloor spreading started around 33 Ma in the northeastern South China Sea (SCS), but varied slightly by 1–2 Myr along the northern continent-ocean boundary (COB). A southward ridge jump of ~20 km occurred around 23.6 Ma in the East Subbasin; this timing also slightly varied along the ridge and was coeval to the onset of seafloor spreading in the Southwest Subbasin, which propagated for about 400 km southwestward from ~23.6 to ~21.5 Ma. The terminal age of seafloor spreading is ~15 Ma in the East Subbasin and ~16 Ma in the Southwest Subbasin. The full spreading rate in the East Subbasin varied largely from ~20 to ~80 km/Myr, but mostly decreased with time except for the period between ~26.0 Ma and the ridge jump (~23.6 Ma), within which the rate was the fastest at ~70 km/Myr on average. The spreading rates are not correlated, in most cases, to magnetic anomaly amplitudes that reflect basement magnetization contrasts. Shipboard magnetic measurements reveal at least one magnetic reversal in the top 100 m of basaltic layers, in addition to large vertical intensity variations. These complexities are caused by late-stage lava flows that are magnetized in a different polarity from the primary basaltic layer emplaced during the main phase of crustal accretion. Deep tow magnetic modeling also reveals this smearing in basement magnetizations by incorporating a contamination coefficient of 0.5, which partly alleviates the problem of assuming a magnetic blocking model of constant thickness and

uniform magnetization. The primary contribution to magnetic anomalies of the SCS is not in the top 100 m of the igneous basement.

## 1. Introduction

The South China Sea (SCS) basin has been traditionally divided into two main subunits, the East and the Southwest Subbasins (Figure 1). The amplitudes and orientations of magnetic anomalies, among other geological/geophysical parameters, differ markedly between these two subbasins, which are divided by a complex boundary called the Zhongnan Fault in between (Figure 1) [Yao, 1995; Li *et al.*, 2008]. The ages of the SCS basin have been investigated for many years based on geophysical data in the central basin [e.g., Taylor and Hayes, 1980, 1983; Briaies *et al.*, 1993; Barckhausen and Roeser, 2004; Barckhausen *et al.*, 2014; Yao *et al.*, 1994; Li and Song, 2012; Song and Li, 2012; Hsu *et al.*, 2004] and on regional major unconformities in the surrounding rift basins [e.g., Taylor and Hayes, 1980, 1983; Wang *et al.*, 2000].

How regional major unconformities identified within the continental margins could reflect tectonic events in the central basin is debated, since in many cases these unconformities cannot be easily traced from the continental margin to the central basin due to common existence of distal uplift near the continent-ocean boundary (COB) [Li *et al.*, 2009, 2013]. Therefore, large uncertainties and different models exist in the estimated opening ages and episodes of the SCS, because of the nonuniqueness of magnetic anomaly identifications [Taylor and Hayes, 1980, 1983; Briaies *et al.*, 1993; Barckhausen and Roeser, 2004; Barckhausen *et al.*, 2014; Yao *et al.*, 1994; Li and Song, 2012; Song and Li, 2012; Hsu *et al.*, 2004]. Different models gave different age estimates (Table 1), and it was uncertain whether the SCS basin experienced primarily a single episode or multiple episodes of extension and seafloor spreading and, if multiple, in what sequence different subbasins evolved [e.g., Taylor and Hayes, 1980; Pautot *et al.*, 1986; Ru and Pigott, 1986; Briaies *et al.*, 1993; Yao *et al.*, 1994; Hayes and Nissen, 2005; Li and Song, 2012]. This problem is further compounded by the fact that all magnetic anomalies previously collected are either shipborne surface-towed or airborne data that are unavoidably attenuated, since the measurement datums were at least 4–5 km above the magnetic source layer.

The early classical works of Taylor and Hayes [1980, 1983] and Briaies *et al.* [1993] estimated that the age of the SCS is from ~32 to 16 or 17 Ma. These age ranges or identified magnetic anomalies were further supported by recent revisits of surface magnetic anomalies based on the updated geomagnetic reversal model [Li and Song, 2012; Song and Li, 2012]. There are also other different models. Hsu *et al.* [2004] argued that magnetic anomalies from part of the northern continental slope could indicate that the early opening of the SCS may have started around 37 Ma, but this part is unlikely to be floored with oceanic crust based on seismic reflections [Li *et al.*, 2007; McIntosh *et al.*, 2013]. Barckhausen and Roeser [2004] concluded that seafloor spreading at the SW rift tip ceased at 20.5 Ma, anomaly 6a1, approximately 4 Ma earlier than interpreted in previous works. Barckhausen *et al.* [2014] again supported this interpretation and argued that spreading at the SCS was in reasonably fast spreading rates, varying from 56 km/Myr in the early stages to 72 km/Myr after the ridge jump to 80 km/Myr in the Southwestern Subbasin.

To better interpret the data, existing and/or known age benchmarks in the SCS are critical. Previous studies have identified some key magnetic anomalies that are characteristic in their amplitudes and are better constrained. Two conspicuous anomalies (M1 and M2 on Figure 1) are previously identified as C8, and are dated as ~27.5 Ma [Taylor and Hayes, 1980, 1983; Briaies *et al.*, 1993], or ~26.4 Ma based on the geomagnetic polarity time scale CK95 of Cande and Kent [1995], or ~26.0 Ma based on the Geomagnetic Polarity Time Scale 2004 of Gradstein *et al.* [2004] [Li and Song, 2012; Song and Li, 2012].

Briaies *et al.* [1993] proposed a small ridge jump occurred after the magnetic anomaly C7, which was originally dated as ~27 Ma. Based on the geomagnetic polarity time scale CK95 [Cande and Kent, 1995], the age of C7 is 24.8 Ma [Li and Song, 2012]. Barckhausen *et al.* [2014] proposed a similar age of 25 Ma. These timings of proposed ridge jump seem to coincide with a prominent unconformity/slump zone of a 2–3 Ma of sedimentary hiatus revealed at Site 1148 of ODP Leg 184 [Wang *et al.*, 2000; Li *et al.*, 2004].

In this study, with our calibrated deep tow magnetic anomalies, we will also examine the spreading rate variations and the existence of the ridge jump event and its age, based on the newly updated Geomagnetic

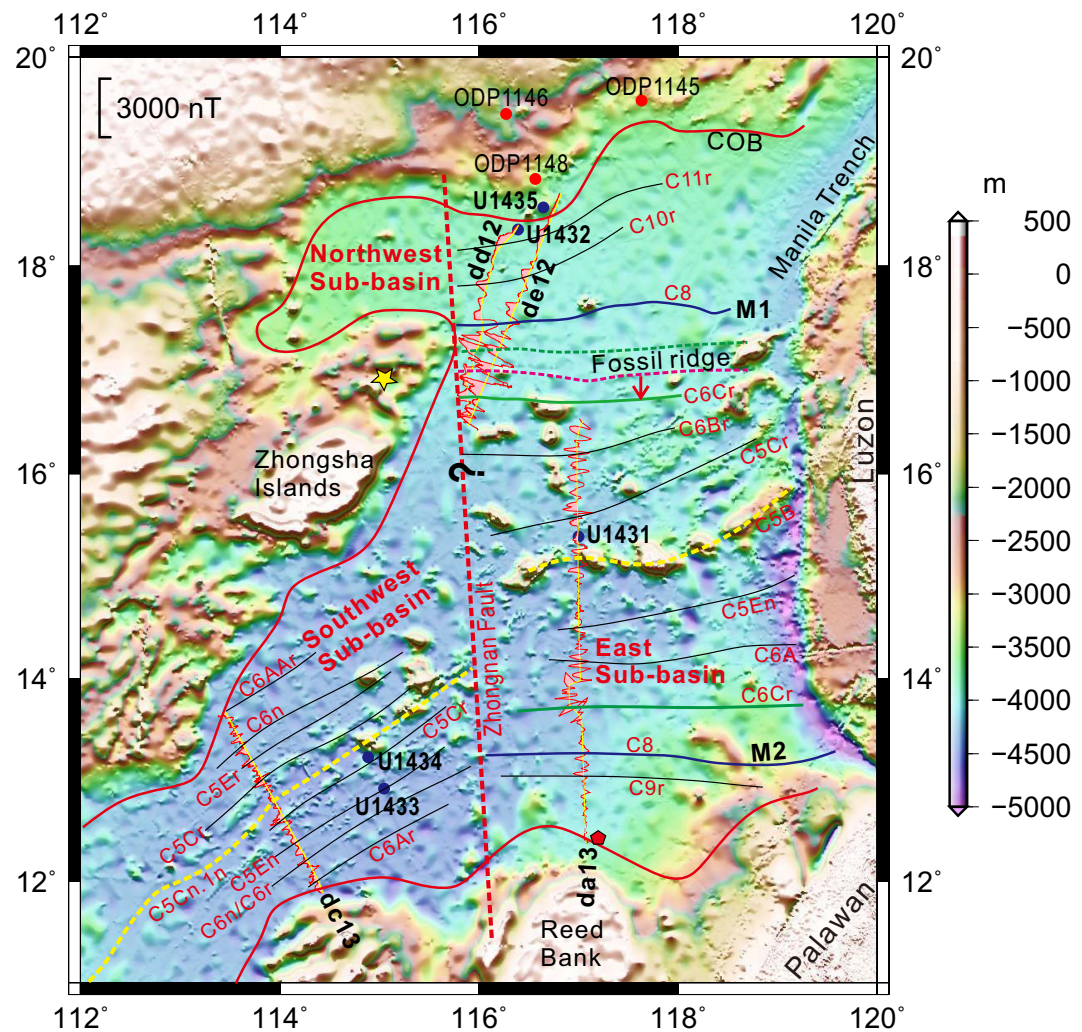


**Figure 1.** Bathymetry map of the SCS showing deep tow magnetic survey tracks and magnetic anomalies. The red pentagon to the north of Reed Bank shows the site where heading variations of ship magnetism were tested in 2013. The yellow star to the north of Zhongsha Islands is the deployment site for the Sentinel seafloor geomagnetic base station. This map shows that the Southwest Subbasin has slightly deeper water depths than the East Subbasin. Blue circles indicate locations of sites drilled during IODP Expedition 349 and red circles are sites drilled during Ocean Drilling Program (ODP) Leg 184. The yellow dashed lines show the final fossil ridges. The pink dashed line marks the place of the ridge jump. The arrow indicates the direction of ridge migration. The solid green line marks the place where the ridge migrated to. The dashed green line is conjugate to the solid green line. Major magnetic anomalies are also shown and marked with anomaly numbers. COB = continent-ocean boundary. Original bathymetry data are from Becker et al. [2009].

Polarity Time Scale 2012 (GPTS2012) [Gradstein et al., 2012]. Two recent endeavors helped move a big step forward in addressing these problems. First, two deep-tow magnetic surveys in the SCS were successfully carried out in 2012 and 2013, respectively, and they represent the first acquisition of high-resolution near-

Table 1. Various Age Estimates of the South China Sea (SCS) Basin From Previous Studies				
Authors	Ages (Ma)	Area of Study	Year of Publication	Data Used
Taylor and Hayes	32–17	East Subbasin	1980, 1983	Magnetic anomaly
Briais et al.	32–16	Central SCS basin	1993	Magnetic anomaly
Yao et al.	42–35	Southwest Subbasin	1994	Magnetic anomaly
Barckhausen and Roeser	31–20.5	Central SCS basin	2004	Magnetic anomaly
Hsu et al.	37–15	Central SCS basin and northeastern SCS	2004	Magnetic anomaly
Ru and Pigott	~55	Southwest Subbasin	1986	Heat flow and bathymetry
	35–36	Northwest Subbasin		
	~32	East Subbasin		



bottom magnetic data offshore China. Altogether, four deep-tow transects were surveyed covering both the East and Southwest Subbasins, and the total length surveyed is 1220 km (Figure 1). By placing the magnetometers closer to the magnetic source layer, we can pick up fine-scale magnetic reversal features that otherwise do not show up clearly on surface-towed profiles.

Furthermore, recently completed International Ocean Discovery Program (IODP) Expedition 349 (26 January 2014 to 30 March 2014) drilled five sites in the central basin of the SCS to study regional geodynamics and oceanic crustal evolution (Figure 1). Three of the five sites (Sites U1431, U1433, and U1434) were cored into the igneous basement near the fossil spreading center where seafloor spreading terminated, and another Site U1435 penetrated through the breakup unconformity proximal to the northern continent-ocean boundary where seafloor spreading started [Expedition 349 Scientists, 2014]. These four sites serve as benchmark points for ages and basement properties that are very much needed to further validate geophysical interpretations.

In this paper, we present results of our studies on these recently acquired deep tow magnetic anomalies and IODP Expedition 349 cores, and revisit the opening models of the SCS. While close to the early proposed model of Taylor and Hayes [1980, 1983] and Briais *et al.* [1993], our results confirm along-strike variation in the onset timing of seafloor spreading, and tune up the age of the ridge jump to be around 23.6 Ma in the East Subbasin. Our calibrated spreading rates, quite opposite to those proposed by Barckhausen *et al.* [2014], throw important new insights into the kinematics of the opening of the basin. Additionally, by measuring and comparing magnetic anomalies at different levels, we are able to examine, with much more confidence, the previously little-known top magnetic layer structures of the oceanic crust. The magnetic measurements from igneous basement cores at Sites U1431, U1433, and U1434 have helped in this regard.

## 2. Deep-Tow Magnetic Surveys

Deep-tow magnetic surveys started in the late 1970s with the development of the Deep Sea Drilling (DSDP) [Greenewalt and Taylor, 1978; Macdonald *et al.*, 1979]. The technique was later extensively applied in surveying global mid-ocean ridges [Tivey, 1996; Perram *et al.*, 1990; Hussenöeder *et al.*, 1996; Pouliquen *et al.*, 2001; Yamamoto *et al.*, 2005]. In recent years, deep-tow magnetic data were further used in discerning hydrothermal vents and their activities [Gee *et al.*, 2001; Tivey and Johnson, 2002; Zhu *et al.*, 2010]. In addition, high-resolution magnetic anomalies were essential for understanding continental breakup [Whitmarsh *et al.*, 1996], magnetic reversal behaviors [Tominaga *et al.*, 2008], and paleointensity variations [Sager *et al.*, 1998; Gee *et al.*, 2000; Granot *et al.*, 2012].

Because this study represents the earliest endeavor in acquiring deep-tow magnetic data by Chinese scientists [Lin *et al.*, 2013], a tremendous amount of time was devoted to designing, building, and testing the deep-towed vehicle, which was assembled at Guangzhou Marine Geological Survey (GMGS). The deep-towed vehicle carried an ultrashort baseline system (USBL), a conductivity-temperature-depth (CTD) logger, an altimeter, and a self-contained digital three-axis magnetoresistor magnetometer (MiniMAG) from Woods Hole Oceanographic Institution. To ensure safe acquisition of at least one copy of magnetic data and real monitoring of the working state of the magnetic system, a SeaSPY proton precession magnetometer was also towed 15 m behind the deep-towed vehicle. Magnetic data from two different systems can be compared with each other and facilitate data processing and interpretation. All these magnetometers were tested and calibrated in the Zhaoqing Geomagnetic Base Station in Guangdong Province before the surveys.

We designed four transects covering nearly all magnetic anomalies of both the East and Southwest Subbasins of the SCS in order to document key points of evolution of the entire basin. The location of the four transects was designed to avoid seamounts and with full consideration of tectonic zonation, magnetic lineation and strength, and ocean currents.

During the surveys, the height of the deep-towed vehicle above the seafloor was collectively controlled by adjusting the length of the opto electric composite cable that connects the deep-towed vehicle with the R/V Haiyang 6 of GMGS, the weight of the deep-towed vehicle, and most critically the cruising speed. The cable length was controlled to be within 7500 m, and the cruising speed varied from 3.334 to 4.074 km/h. The heights of the magnetometers were kept mostly between 200 and 500 m above the seafloor (Figure 2).

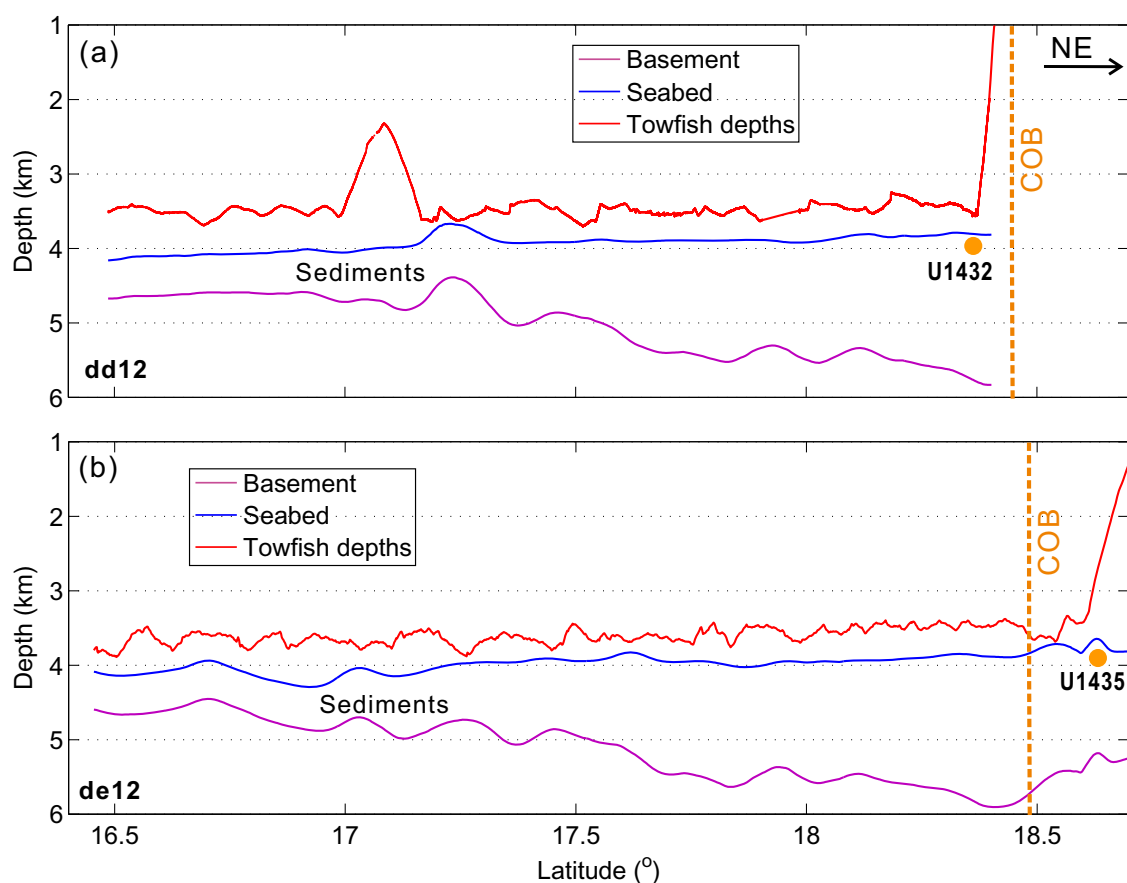


**Figure 2.** Estimated basement depths from seismic profiles and towfish depths from deep tow altimeter readings. (a) Transect dd12; (b) Transect de12. COB = continent-ocean boundary.

Because of the low cruising speed required, it took R/V Haiyang 6 nearly a month of total work at sea to finish 1220 km of deep tow magnetic survey along four transects: dd12 and de12 acquired in 2012, and dc13 and da13 surveyed in 2013 (Figure 1).

Meanwhile, a SeaSPY proton precession magnetic gradiometer was towed ~350 m behind the ship to record magnetic anomalies from the sea surface, which are compared to deep tow magnetic anomalies to better calibrate data at different levels. The two magnetometers in the gradiometer were spaced 80 m apart. Although not used and presented in this paper, three-axis shipborne magnetic data were also acquired during our surveys by installing fluxgate magnetometers on the mast and GPS antennas.

There are several inland magnetic base stations around the SCS that can provide diurnal corrections to our surveyed data. We collected their data for data processing. We also deployed a Sentinel seafloor geomagnetic base station in the Zhongsha Islands at a water depth of 2789 m (Figure 1). The station worked well during our survey in 2013.

### 3. Magnetic Data Processing

First, magnetic, navigation, and attitude data are extracted from their respective raw data files and they are then merged together into one file for each transect. Navigation data are then corrected from the ship positions to the positions of magnetometers based on the recorded lengths of the cables, assuming that the cable runs antiparallel to the heading direction. When the underwater positioning system works well, no navigation corrections are needed for deep-towed magnetometers.

To remove the theoretical geomagnetic field from the observed data, we apply at 0 m altitude, the software Geomag 7.0 and the International Geomagnetic Reference Field (IGRF), which is a spherical harmonic

degree 13 model [International Association of Geomagnetism and Aeronomy (IAGA), Working Group V-MOD, 2010]. For deep-towed measurements, the software Geomag cannot give geomagnetic intensities for negative altitudes below the sea level, but we find out that the small differences by using geomagnetic intensity at 0 m altitude do not present an issue in magnetic modeling and calibration. For diurnal corrections, we refer data from Zhaoqing and Qiongzong Geomagnetic Base Stations in Guangdong Province and Hainan Island, respectively (23.093°N, 113.344°E and 19.000°N, 109.800°E), for the year 2012 survey, and for the year 2013 survey, we use data from Dalat Geomagnetic Observatory in Vietnam (11.945°N, 108.482°E) for surface-towed data and from the seafloor geomagnetic base station (17.039°N, 115.000°E) for deep-towed data. We find that diurnal corrections are normally small, mostly within  $\pm 50.0$  nT. These external field corrections have longer wavelengths and lower amplitudes than most deep-tow anomalies, and therefore, make little change in the anomaly sequence character [Tominaga *et al.*, 2008].

After all the above corrections, the data are further smoothed with a 100 m wide moving window to remove very short wavelength errors and then resampled to larger sampling intervals. Finally, the magnetic anomalies are projected to a common azimuth for each transect. The final processed data are shown in Figures 3–5. Data from both levels are clearly synchronized in their trends. This demonstrates the advantage of deep tow magnetic anomalies and also validates the effectiveness of our data acquisition and processing scheme.

To further see the correlation between surface and deep tow magnetic anomalies, we carry out upward continuation on the deep tow magnetic anomalies from the uneven deep tow level to the sea level using the frequency domain chessboard method [Cordell, 1985; Cordell *et al.*, 1993; Phillips, 1997]. The upward continued deep tow magnetic anomalies match remarkably well with the anomalies measured at the sea level (Figure 6), and can be used to provide a reference in correlating smaller anomalies [Sager *et al.*, 1998; Tominaga *et al.*, 2008].

## 4. Magnetic Anomaly Modeling and Age Constraints

### 4.1. Model Construction and Parameters

Before constraining SCS crustal ages based on deep tow magnetic anomalies, we need to define the continent-ocean boundary (COB) to avoid modeling anomalies that may not be associated with oceanic crust (Figures 7 and 8). From comprehensive magnetic, gravimetric, and reflection seismic data analyses, Li and Song [2012] found that the COB corresponds roughly with a transitional boundary in free-air gravity anomalies between mostly positive gravity anomalies in the central oceanic basin and grossly negative gravity anomalies in the extended and subsided transitional continental crust (Figure 7). The COB so defined is close to other interpretations [Nguyen *et al.*, 2004; Braitenberg *et al.*, 2006; Franke *et al.*, 2011]. Within the area confined by the COB, the regional magnetic anomaly map based on the shipborne and airborne magnetic dataset compiled by Geological Survey of Japan and Coordinating Committee for Costal and Offshore Geoscience Programs in East and Southeast Asia (CCOP) [Ishihara and Kisimoto, 1996], shows typical alternating magnetic reversal patterns (Figure 8).

On or near most segments of our deep-tow magnetic survey lines, we have multichannel reflection seismic profiles to constrain the depths to the magnetic sources (igneous basement) [Li *et al.*, 2010; Ding *et al.*, 2013]. The thickness of sediments can be estimated from the time-depth curves obtained from sonic logging at Site 1148 from ODP Leg 184 [Wang *et al.*, 2000; Li *et al.*, 2008] and at IODP Site U1433 from Expedition 349 [Expedition 349 Scientists, 2014]. Where seismic constraints are not possible, we either use a gradual change in the basement between two controlling depth points or apply the average basement depths based on adjacent data.

To simulate magnetic anomalies, we use the MATLAB based software MODMAG [Mendel *et al.*, 2005], which is a versatile tool that can accommodate varying spreading rates and asymmetric spreading possibly alternating with axial jumps. The computing algorithm of the software is based on Talwani and Heirtzler [1964].

Previous studies suggested that the spreading rates of the SCS are low to intermediate [Taylor and Hayes, 1980, 1983; Briais *et al.*, 1993; Song and Li, 2012]. In these scenarios, off-axis intrusions or late-stage lava flows that move horizontally for a long distance may contaminate preexisting polarity stripes [Tisseau and Patriat, 1981; Mendel *et al.*, 2005]. The deeper part of oceanic crust also cools and becomes magnetized later

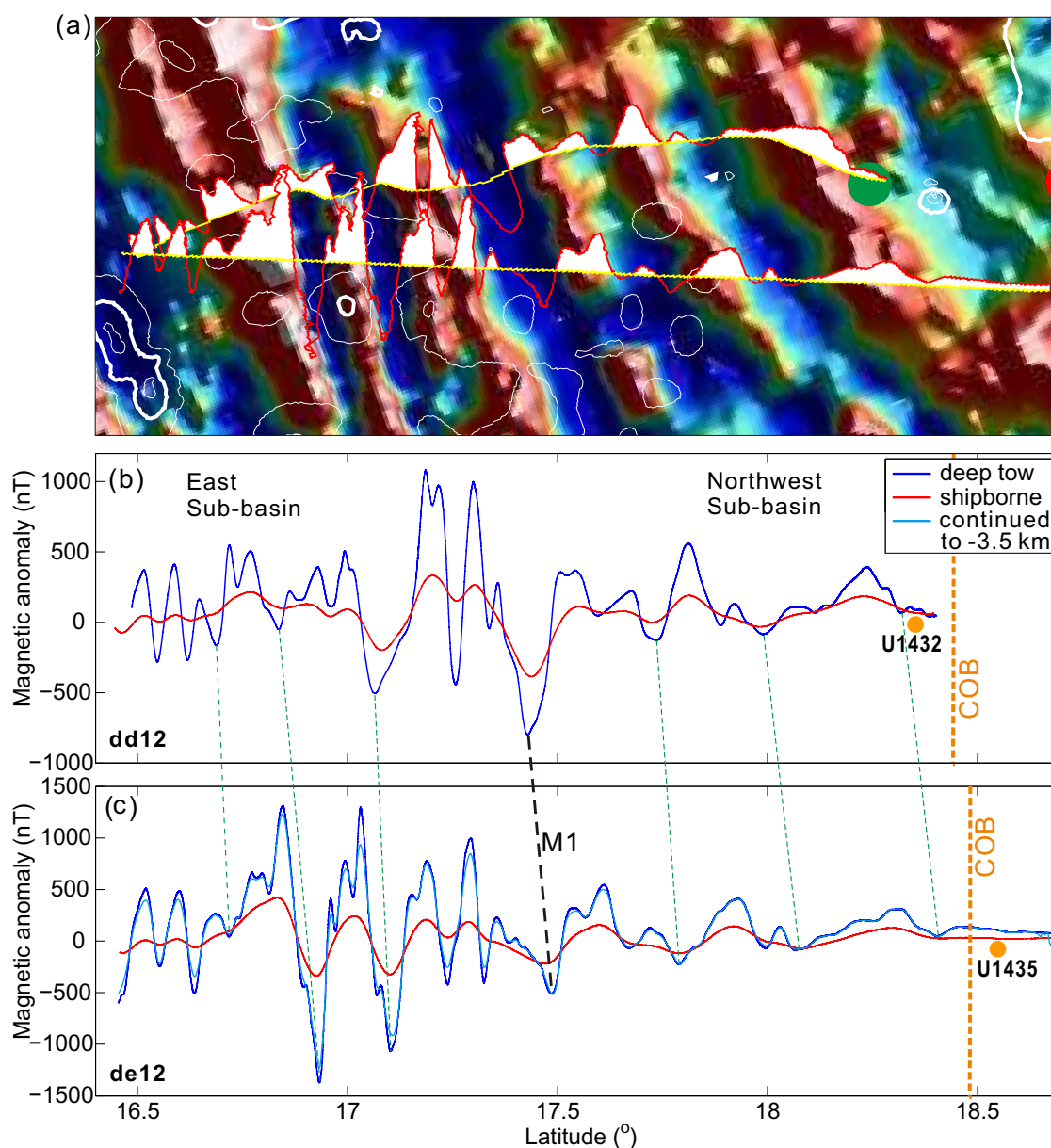


**Figure 3.** Comparison between deep tow and surface magnetic anomalies, and correlation between transects dd12 and de12 in the northern part of the SCS. (a) Deep tow magnetic anomalies overlaid on a regional magnetic anomaly map based on airborne and shipborne magnetic data; (b) magnetic anomalies of transect dd12; (c) magnetic anomalies of transect de12. COB = continent-ocean boundary.

than the shallower part [Kidd, 1977]. MODMAG is capable of dealing with these problems by forward modeling with a fictitious spreading rate that is slower than the real spreading rate, based on the method of *Tis-seau and Patriat* [1981]. By assigning different contamination coefficients  $R$  ( $0 < R \leq 1$ , with 1 for no contamination), the magnetic source blocks are narrowed corresponding with the fictitious spreading rate before modeling, and are put back to their original position after computation [Mendel et al., 2005].

The measurement datum assumed by MODMAG needs to be constant, but our measurements are made on uneven surfaces (Figures 4 and 5). As we show in Figure 6, anomalies of transect de12 upward continued to the sea level from the uneven deep tow level have an excellent match to anomalies measured at the sea level, suggesting that unevenness in observation level is not problematic. We can test again on transect de12 how this unevenness affects our observations by upward continuation from the uneven observation surface to an adjacent level, and we find that the magnetic anomalies after upward continuation to 3.5 km are very close to the original observation (Figure 3c). This shows that unevenness in our observation does



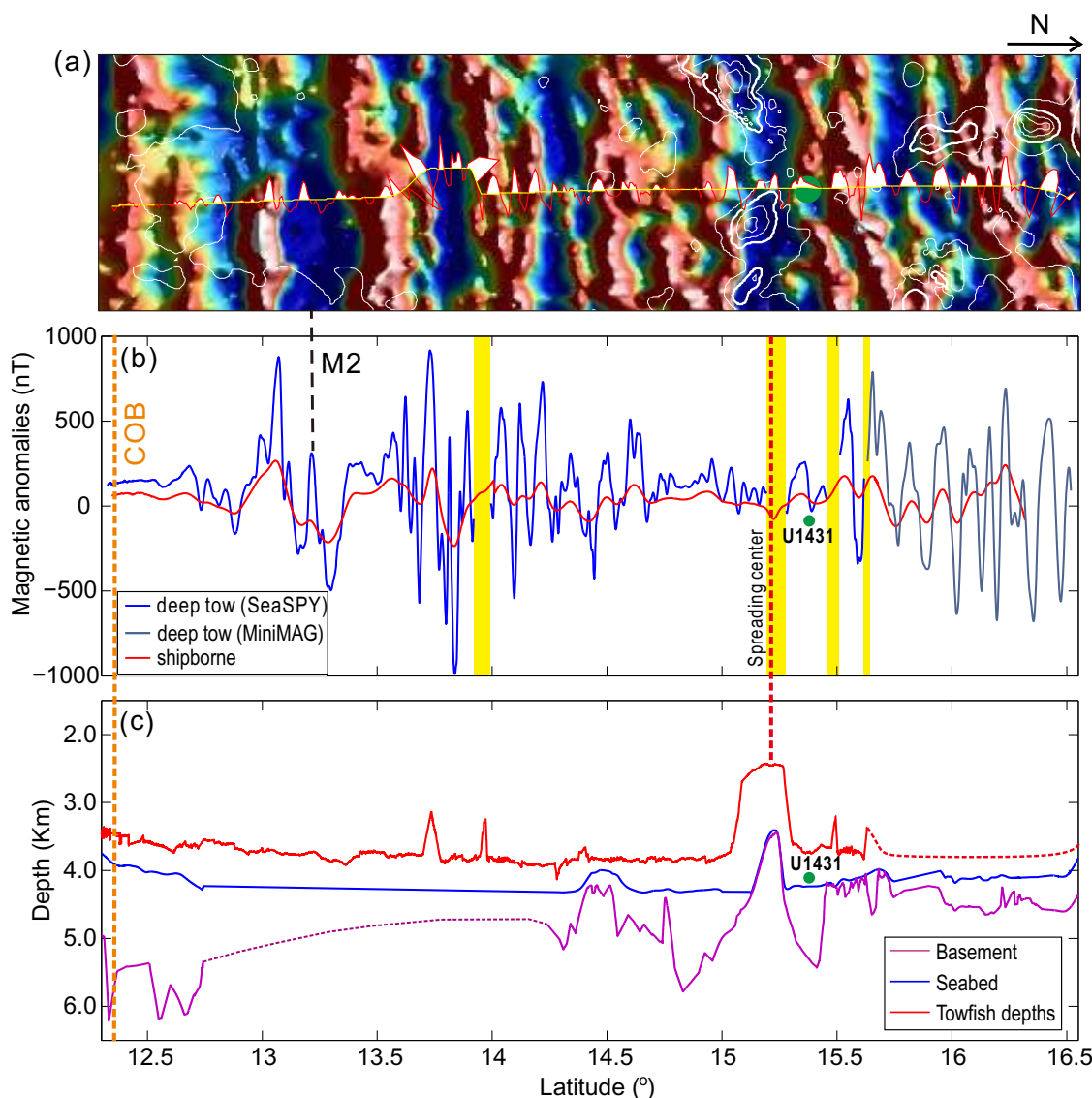


**Figure 4.** Magnetic anomalies acquired along transect da13. (a) Deep tow magnetic anomalies overlaid on a regional magnetic anomaly map based on airborne and shipborne magnetic data; (b) magnetic anomalies of transect da13; (c) estimated basement depths from seismic profiles and towfish depths from deep tow altimeter readings along transect da13. Vertical yellow bands show data gaps in deep tow magnetic anomalies.

not change the magnetic anomaly patterns and have no effects on data calibration. We therefore opt to use the originally observed instead of leveled anomalies in data calibration.

We adopt the most up-to-date magnetic polarity reversal models from the Geomagnetic Polarity Time Scale 2012 (GPTS2012) [Gradstein *et al.*, 2012]. Other information needed for the modeling include ambient magnetic field components (inclination and declination), spreading direction, azimuth of the profile, depth of source layer, and mean latitude and strike of magnetic bodies at the time of ridge formation (Table 2). These parameters vary from line to line but can be easily determined from geological and geophysical survey data and geographical data. The mean ambient magnetic inclinations and declinations are based on the IGRF model [International Association of Geomagnetism and Aeronomy (IAGA), Working Group V-MOD, 2010]. The opening of the SCS is accompanied with southward movement of parts of formed oceanic crust, and it is necessary to compute the inclination and declination of remanent magnetization vector based on mean latitude and strike of magnetic bodies at the time of ridge formation. Assuming a geocentric axial dipole, the remanent inclinations ( $I_r$ ) are calculated from the mean paleolatitudes ( $\lambda$ ) based on the following equation [e.g., Mendel *et al.*, 2005]

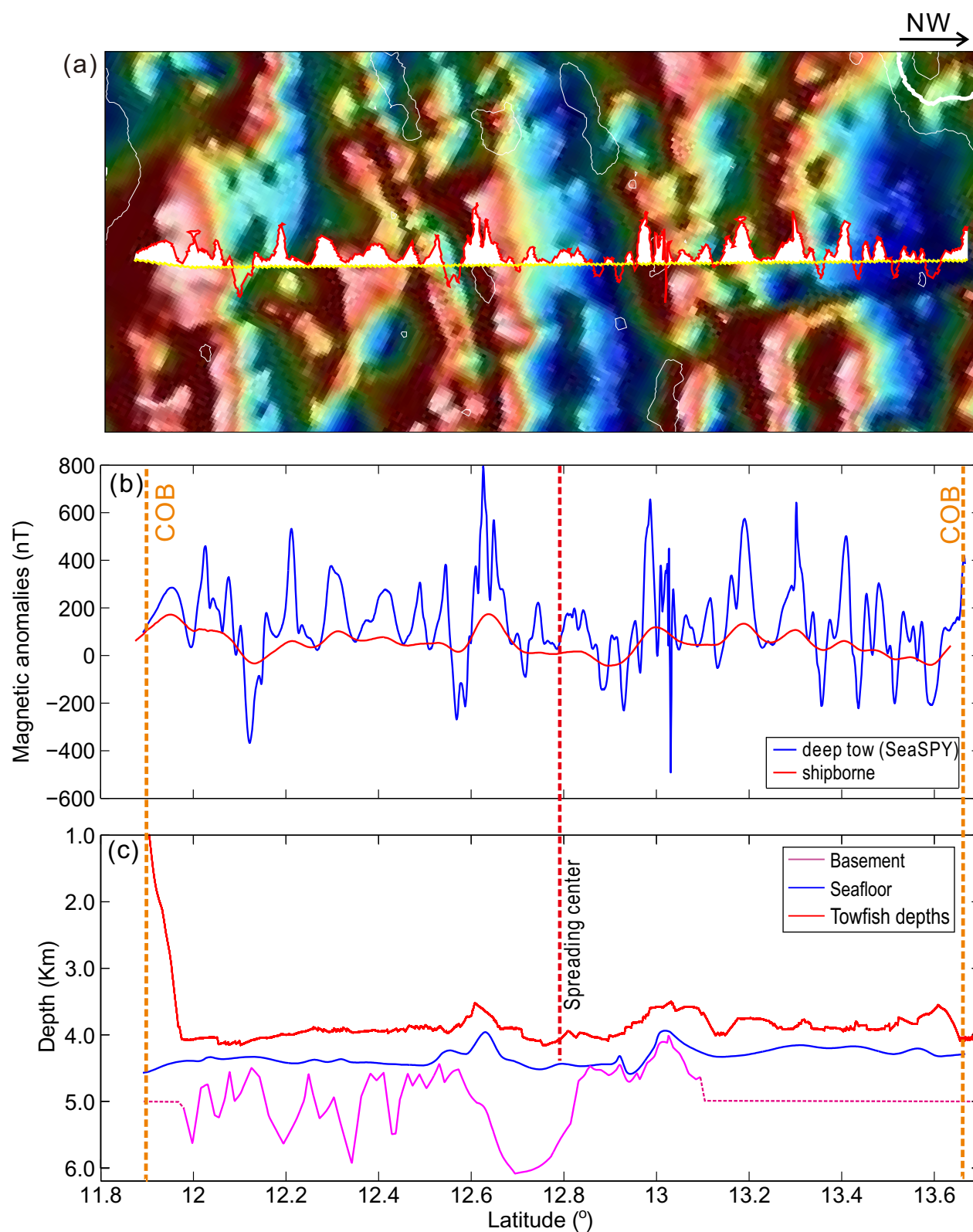


**Figure 5.** Magnetic anomalies acquired along transect dc13. (a) Deep tow magnetic anomalies overlaying on regional magnetic anomaly map based on airborne and shipborne magnetic data; (b) magnetic anomalies of transect dc13; (c) estimated basement depths from seismic profiles and towfish depths from deep tow altimeter readings along transect dc13.

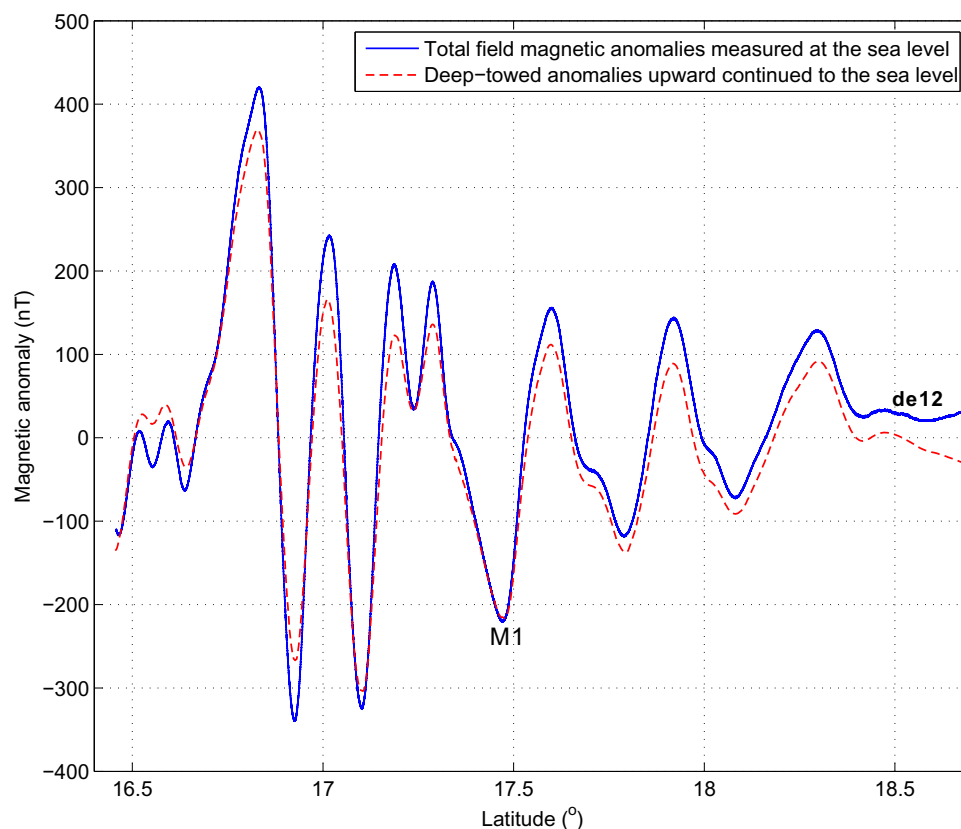


**Figure 6.** Comparison between surface magnetic anomalies and deep tow magnetic anomalies upward continued to the sea level.

$$\tan(lr) = 2 \tan(\lambda). \quad (1)$$

Paleolatitudes are assessed from the plate movement and the virtual geomagnetic pole of the plate. We keep a constant magnetic layer thickness of 0.5 km and assume that the average crustal magnetization is 5 A/m. Keeping these parameters constant allows more robust estimates of spreading rates and ages, which are the main objectives of this study.

#### 4.2. Modeling

In situ measurements of basement ages are crucial for ground truthing the above inferred ages and providing new benchmarks for understanding the kinematics of seafloor spreading. Recently, completed IODP Expedition 349 drilled through the sediment-basement interface and recovered oceanic basalts at three sites, U1431, U1433, and U1434 (Figure 1). Radiometric age dating on basalts is ongoing; however, preliminary microfossil age constraints are obtained at/near the sediment-basement interface and/or from interflow sediments between basaltic units (Table 3) [Expedition 349 Scientists, 2014]. Our deep tow transects either pass through or are close to Sites U1431, U1432, and U1435 in the East Subbasin so that data from these IODP sites provide crucial age constraints. In the Southwest Subbasin, transect dc13 is about 100 km away to the southwest of Sites U1433 and U1434, but based on the regional magnetic anomaly map (Figure 8), the projected positions of these sites on the transect dc13 can be determined.

Nevertheless, in our study, we have always relied highly on the high-quality magnetic anomaly data in assessing ages. The ages from IODP sites are used as referencing points, but by no means have these points been assigned fixed ages in our modeling. In other words, we do not force our modeled ages at the IODP sites to be identical to the microfossil determined ages. Rather, we follow the guidance of magnetic anomalies, but check if the microfossil determined ages fall into our modeled age intervals between controlling points. It would be alarming if the modeled ages are way off the microfossil determined ages.



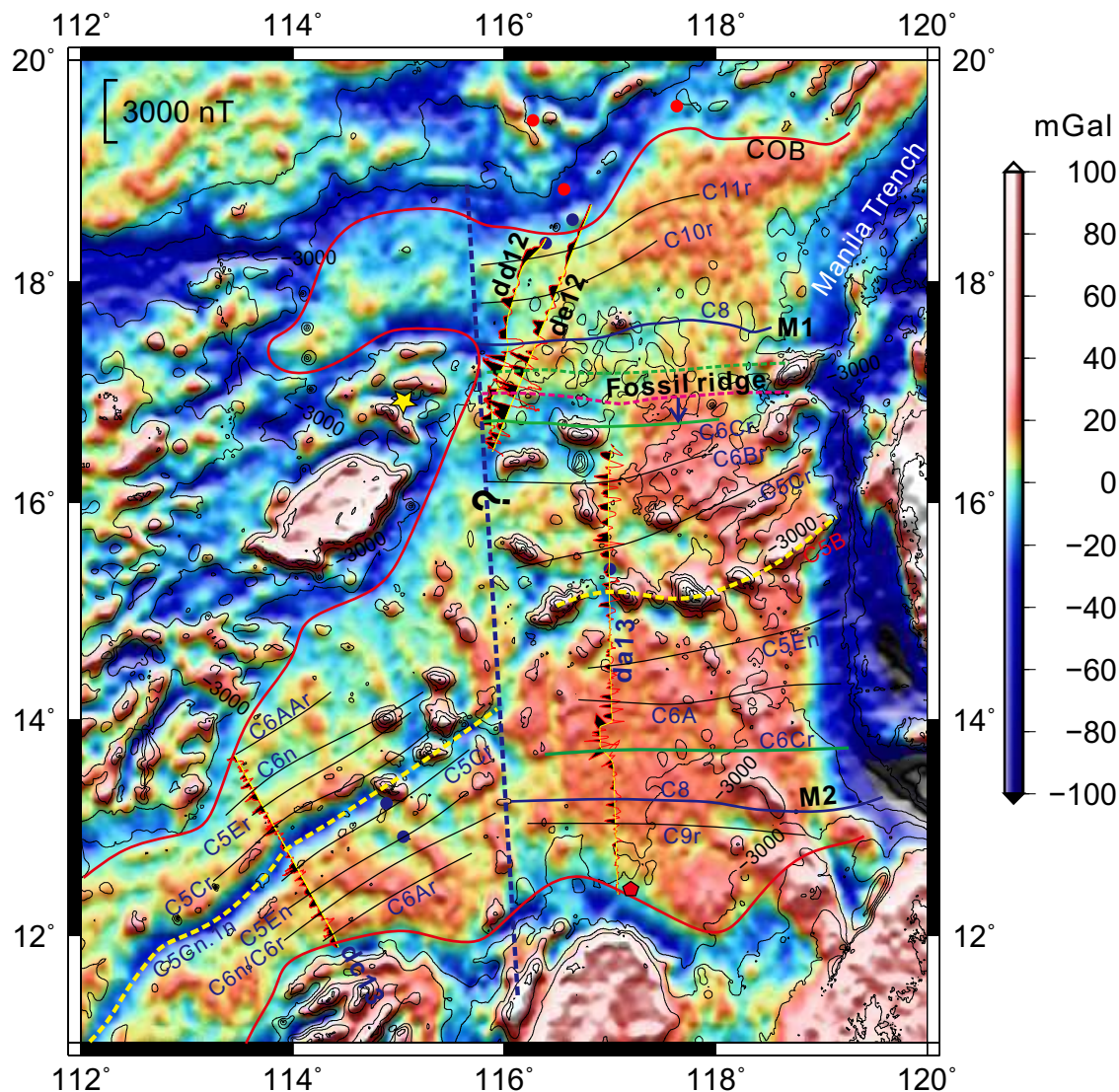


**Figure 7.** Free-air gravity anomaly map of the SCS showing deep tow magnetic survey tracks and magnetic anomalies. The yellow dashed lines show the final fossil ridges. The pink dashed line marks the place of the ridge jump. The arrow indicates the direction of ridge migration. The solid green line marks the place where the ridge migrated to. The dashed green line is conjugate to the solid green line. Major magnetic anomalies are also shown and marked with anomaly numbers. See Figure 1 for more annotations. Original gravity data are from Sandwell and Smith [2009] and Sandwell et al. [2013].

#### 4.2.1. East Subbasin

Transects dd12 and de12 in the northern part of the East Subbasin are subparallel to each other and can be easily correlated (Figures 1, 3, and 8). On both transects, we observe a sharp magnetic boundary between anomalies of low amplitudes to the north and of high amplitudes to the south (denoted as M1 on Figures 1, 3, and 8). This boundary shows a characteristic magnetic pattern with large negative amplitude that is best modeled if it is assigned as the boundary between magnetic chrons C8r and C8n, which has an age of  $\sim 26.0$  Ma according to GPTS2012.

The major unconformity dated to  $\sim 33$  Ma recovered at IODP Site U1435 is inferred to represent the earliest regional seafloor spreading and rapid thermal subsidence that triggered changes from shallow marine to deep marine sedimentary environments. From regional correlation of magnetic anomalies, the oldest oceanic crust appears to be further northeast of transects dd12 and de12 (Figure 8). Therefore, the oldest ages revealed by these two transects near the COB should be younger than 33 Ma. Based on our forward modeling, we find that the onset of seafloor spreading locally near Site U1432 began at about 31.5 Ma, which is about 1.5 Myr later than the earliest regional onset of seafloor spreading (Figures 8 and 9).



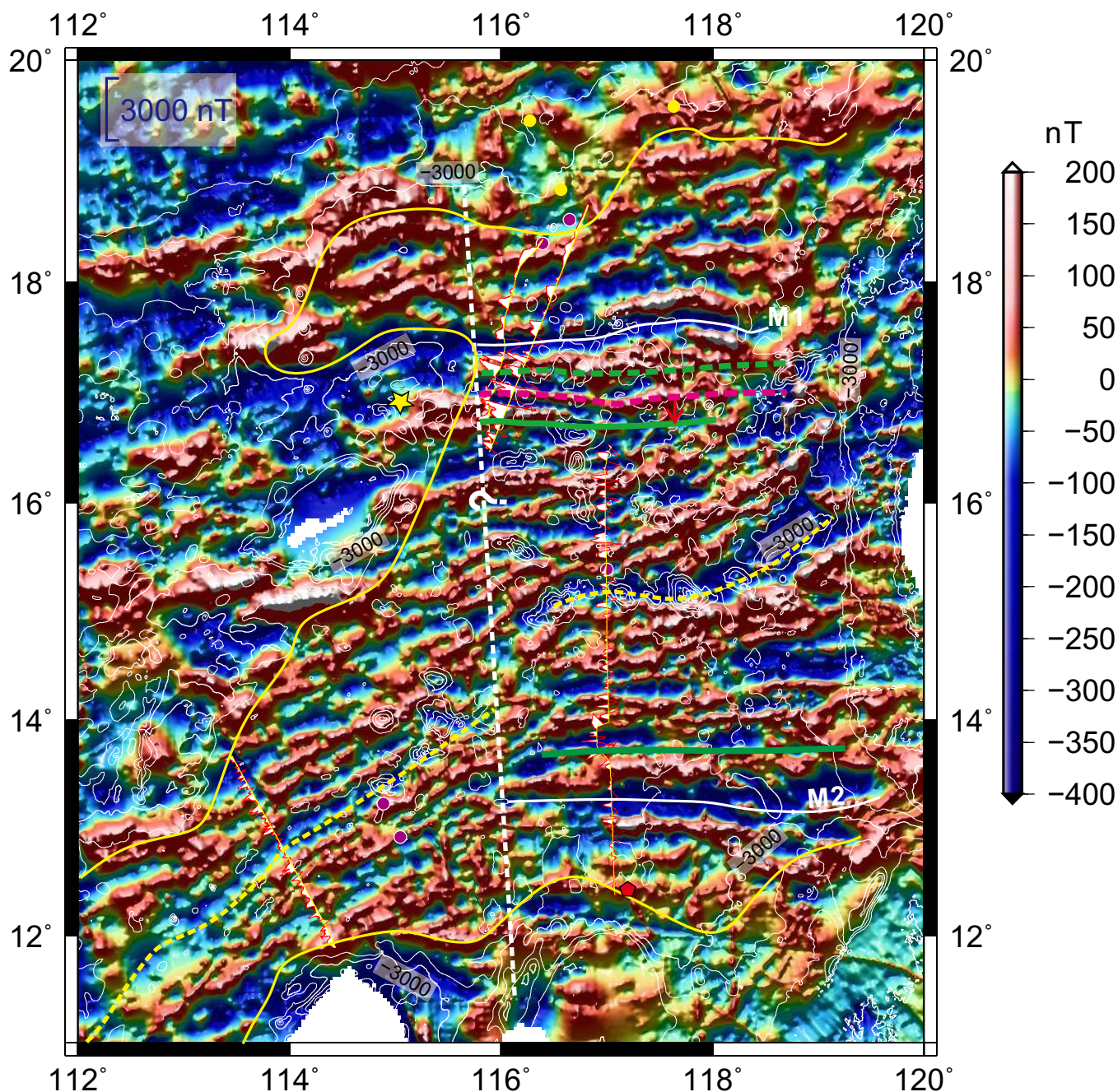


**Figure 8.** Magnetic anomaly map of the SCS showing deep tow magnetic survey tracks and magnetic anomalies. The yellow dashed lines show the final fossil ridges. The pink dashed line marks the place of the ridge jump. The arrow indicates the direction of ridge migration. The solid green line marks the place where the ridge migrated to. The dashed green line is conjugate to the solid green line. Purple circles indicate locations of sites drilled during IODP Expedition 349, and yellow circles are sites drilled during Ocean Drilling Program (ODP) Leg 184. Major magnetic anomalies are also shown and marked with anomaly numbers. Original magnetic data are from *Ishihara and Kisimoto* [1996].

**Table 2.** Some of the Parameters Used in Our Forward Magnetic Modeling

Line Name	Ambient Inclination (°)	Ambient Declination (°)	Remanent Inclination (°)	Remanent Declination (°)	Line Azimuth (°)	Level of Observation (km)	Paleolatitude (°)	Paleostrike (°)
dd12	22.8	−1.87	32.2	−1.87	12.3	3.75	17.5	90
de12	22.8	−1.87	32.2	−1.87	21.9	3.5	17.5	90
da13	17.5	−1.5	28.2	−1.5	0.0	3.5	15.0	90

**Table 3.** Estimated Ages of Sediment Lying Directly on (Site U1434) or Within Basement (Sites U1431 and U1433), and Estimated Age of Breakup Unconformity at Site U1435, Based on Biostratigraphy [Expedition 349 Scientists 2014]<sup>a</sup>

Site	Location	Biostratigraphic Datums	Inferred Age Range	For
U1431	15°22.5'N, 117°0.0'E ~15 km off ridge axis in East Subbasin	LO <i>Didymocyrtis prismatica</i> (16.73 Ma) FO <i>Calocyclus costata</i> (17.59 Ma)	16.7–17.5 Ma. From interflow sediments	Basement
U1433	12°55.1'N, 115°02.8'E ~50 km off ridge axis in Southwest Subbasin	LO <i>Triquetrorhabdulus carinatus</i> (18.28 Ma) FO <i>Stichocorys delmontensis</i> (20.6 Ma)	18–21 Ma. From sediments attached to basalt	Basement
U1434	13°11.5'N, 114°55.4'E ~15 km off ridge axis in Southwest Subbasin	FO <i>Discoaster kugleri</i> (11.9 Ma)	12–18 Ma. From sediments overlying the basement	Basement
U1435	18°33.3'N, 116°36.6'E Near continent-ocean boundary	LO <i>Coccolithus formosus</i> (32.92 Ma) LO <i>Clausiococcus distichus acme</i> (33.43 Ma)	~33 Ma	Breakup unconformity

<sup>a</sup>Notes: LO = last occurrence; FO = first occurrence.

Early studies suggested a ridge jump around the anomaly associated with chron C7 [Briais *et al.*, 1993], which could have caused the slightly wider half basin to the north of the fossil axial ridge than to the south. Although this geometrical asymmetry could be explained by asymmetrical spreading rates across the axial ridge, by integrated analyses with transect da13 (Figure 10), we now also prefer a ridge jump around 23.6 Ma as this arrangement gives the best matches between modeled and observed anomalies (Figures 8–10). The timing of this ridge jump varies slightly from 23.5 to 23.85 Ma based on our modeling of the three transects in the East Subbasin, and the distance of the jump is about 20 km and also varies slightly from place to place.

Transect da13 traverses the crust in the central basin that is not covered by transects dd12 and de12. This allows modeling of magnetic anomalies over the entire basin without large gaps. During the acquisition of data along transect da13, the cable connecting the deep-towed vehicle and the SeaSPY magnetometer developed a leakage problem and had to be fixed several times. This caused narrow data gaps in the SeaSPY data and early pullout of the SeaSPY magnetometer, but both deep-towed MiniMAG and surface-towed magnetometers worked well and recorded excellent data that complement SeaSPY magnetometer readings (Figure 11).

In a central Pacific study, Barckhausen *et al.* [2013] compared biostratigraphically determined ages of sediments directly overlying the igneous oceanic crust with confirmed crustal ages based on magnetic anomaly identifications, and found that consistently the sediment ages are 1–3 Myr younger than the magnetically derived ages. In our case, here at IODP Site U1431, which is about 15 km away from the fossil spreading center (Figures 1 and 11), the datable age of sediment above the basement is just about 13 Ma. However, radiolarians were found here from interflow sediments between two basaltic units of the basement, and they were picked from the 63  $\mu$ m size fraction and examined using scanning electron microscope (SEM). The presence of *Didymocyrtis prismatica* and *Calocyclus costata* gives an estimated biostratigraphy age of ~16.7–17.5 Ma (Table 3), which is considered more representative of the age of the underlying basement [Expedition 349 Scientists, 2014]. The terminal age of the ridge is expected to be a little younger than this age range. Our modeling suggests that the optimal terminal age in the East Subbasin is ~15.0 Ma (Figure 11).

To the south of the axial ridge, M2 is the sharp magnetic boundary thought to be conjugate to M1. From our modeling, we notice that the same boundary between magnetic chrons C8r and C8n creates a positive magnetic anomaly between two large negative anomalies here. This is different from the single large negative anomaly caused by the same chron boundary to the north of the axial ridge, because of their opposite relative positions of magnetic chrons C8r and C8n; chron C8n is located to the south of chron C8r north of the fossil ridge, but to the south of the fossil ridge chron C8n is located north of chron C8r (Figures 9–11). With this character, we can easily identify the location of M2, which provides a definitive age control (Figure 11).

Our modeling results based on the three transects in the East Subbasin indicate that the full spreading rate was higher at the beginning of seafloor spreading from ~32 to ~29 Ma (Figure 12). The spreading rate dropped to a low of ~25 km/Myr on average from ~29 to ~26 Ma. Studies in other parts of the oceanic basin have always indicated abrupt changes in spreading rate [Müller *et al.*, 2008]. The relatively fast

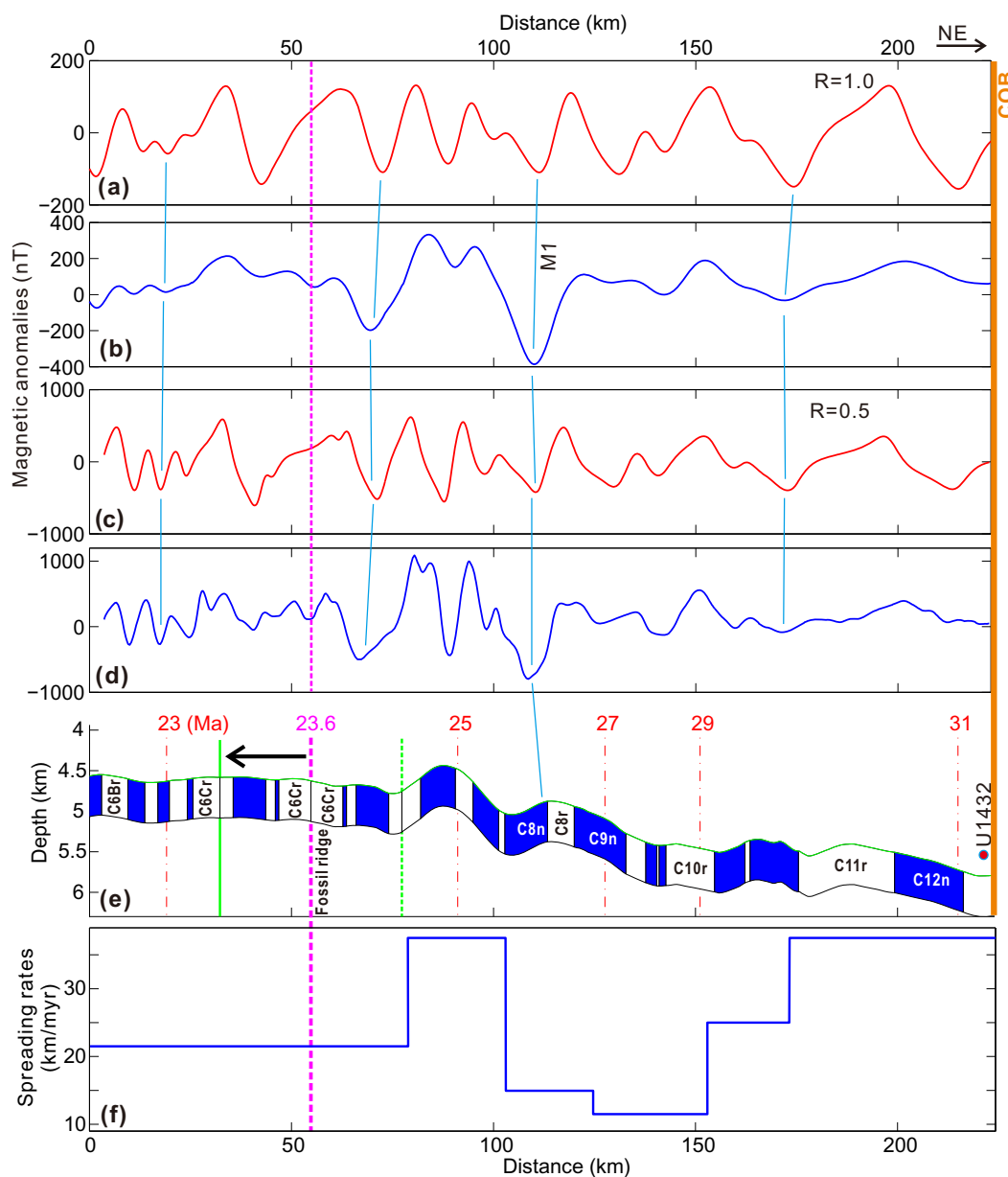


**Figure 9.** Calibration between modeled and observed magnetic anomalies of transect dd12. (a) Modeled surface magnetic anomalies; (b) observed surface magnetic anomalies; (c) modeled deep tow magnetic anomalies; (d) observed deep tow magnetic anomalies; (e) the basement magnetization model (blue color indicating normal magnetization). The pink dashed line marks the place of the ridge jump. The arrow indicates the direction of ridge migration. The left solid green line marks the place where the ridge migrated to. The right dashed green line is conjugate to the left solid green line, and they together show the segment with repeating magnetic blocks due to the ridge jump. (f) Half spreading rates that were used to construct the model.  $R$  = contamination coefficient; COB = continent-ocean boundary.

spreading rates at the first several million years after the onset of seafloor spreading in the SCS could reflect the active lithospheric breakup and mantle upwelling. The basement variations in the SCS also indicate large variations in the spreading rate; the older part of the oceanic basement closer to the northern continental margin is rather featureless, but the area close to the relict spreading center and the Southwest Sub-basin show many basement ridges [Li *et al.*, 2010, 2013]. These changes in basement structures from being smooth to rough could be caused by spreading rate variations from being relatively fast at the beginning to relatively slow near the end of seafloor spreading in the East Subbasin.

The magnetic anomalies M1 and M2 also appear as a boundary in the spreading rate; from these anomalies to the ridge jump around 23.6 Ma, the spreading rate was the highest, peaking at about 75 km/Myr. After



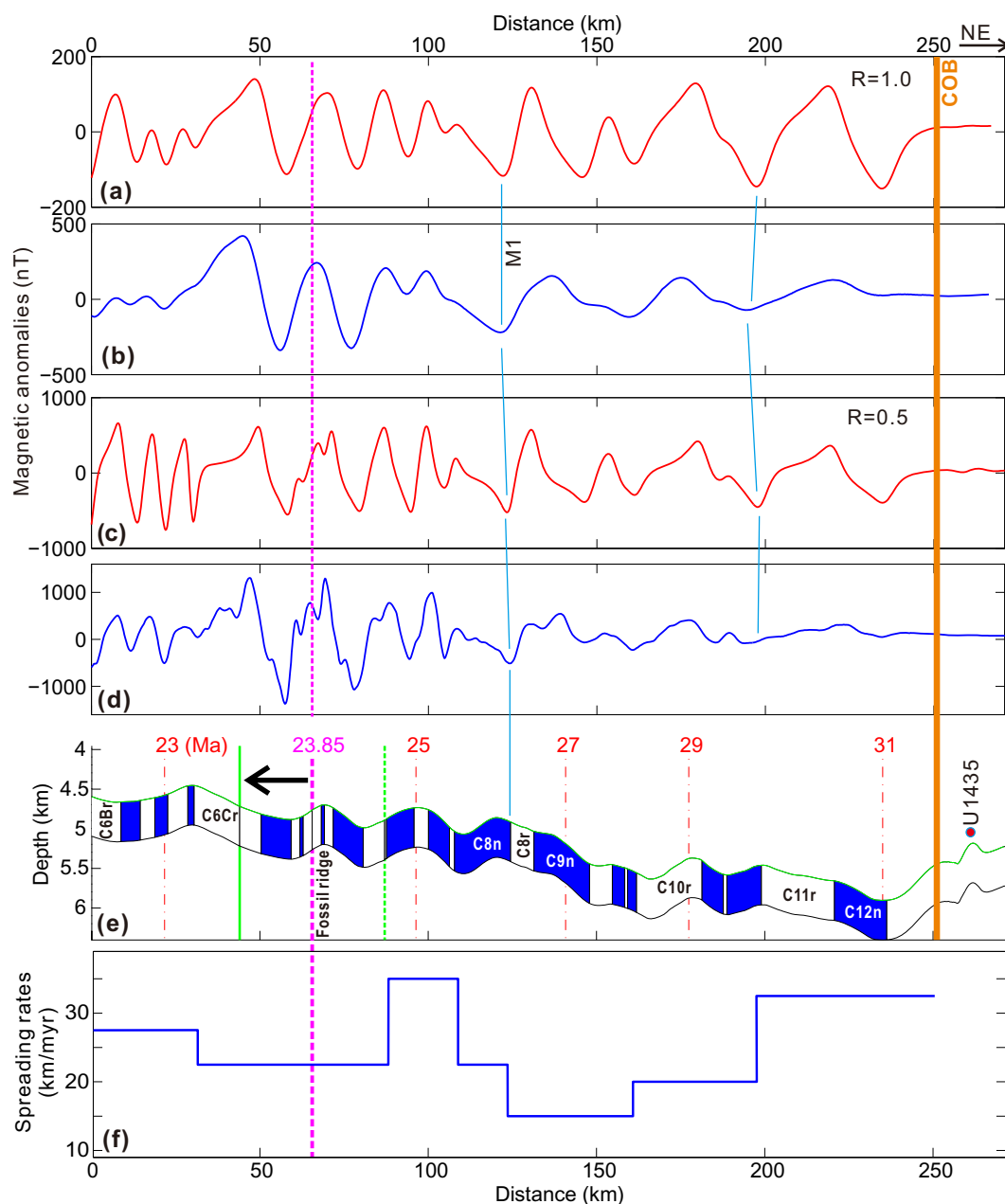


**Figure 10.** Calibration between modeled and observed magnetic anomalies of transect de12. (a) Modeled surface magnetic anomalies; (b) observed surface magnetic anomalies; (c) modeled deep tow magnetic anomalies; (d) observed deep tow magnetic anomalies; (e) the basement magnetization model (blue color indicating normal magnetization). The pink dashed line marks the place of the ridge jump. The arrow indicates the direction of ridge migration. The left green line marks the place where the ridge migrated to. The right dashed green line is conjugate to the left solid green line, and they together show the segment with repeating magnetic blocks due to the ridge jump. (f) Half spreading rates that were used to construct the model.  $R$  = contamination coefficient; COB = continent-ocean boundary.

the ridge jump, the spreading rate was variable but generally decreasing from  $\sim 50$  to  $\sim 35$  km/Myr. This second peak in spreading rate around 25 Ma could be associated with the onset a second seafloor spreading event in the Southwest Subbasin and the identified ridge jump. Intensified regional tectonics also caused a regional unconformity and depositional hiatus at the Oligocene-Miocene boundary in the northern continental margin [Wang *et al.*, 2000]. The gradually decreasing spreading rate after the second peak can be explained by the slowing down in the mantle convection toward the dying of the seafloor spreading process.

We observe small but perceivable along-strike variations in tectonic timing and spreading rate. At different profiles, the initial onset of seafloor spreading and age of the ridge jump are not exactly the same. Figure



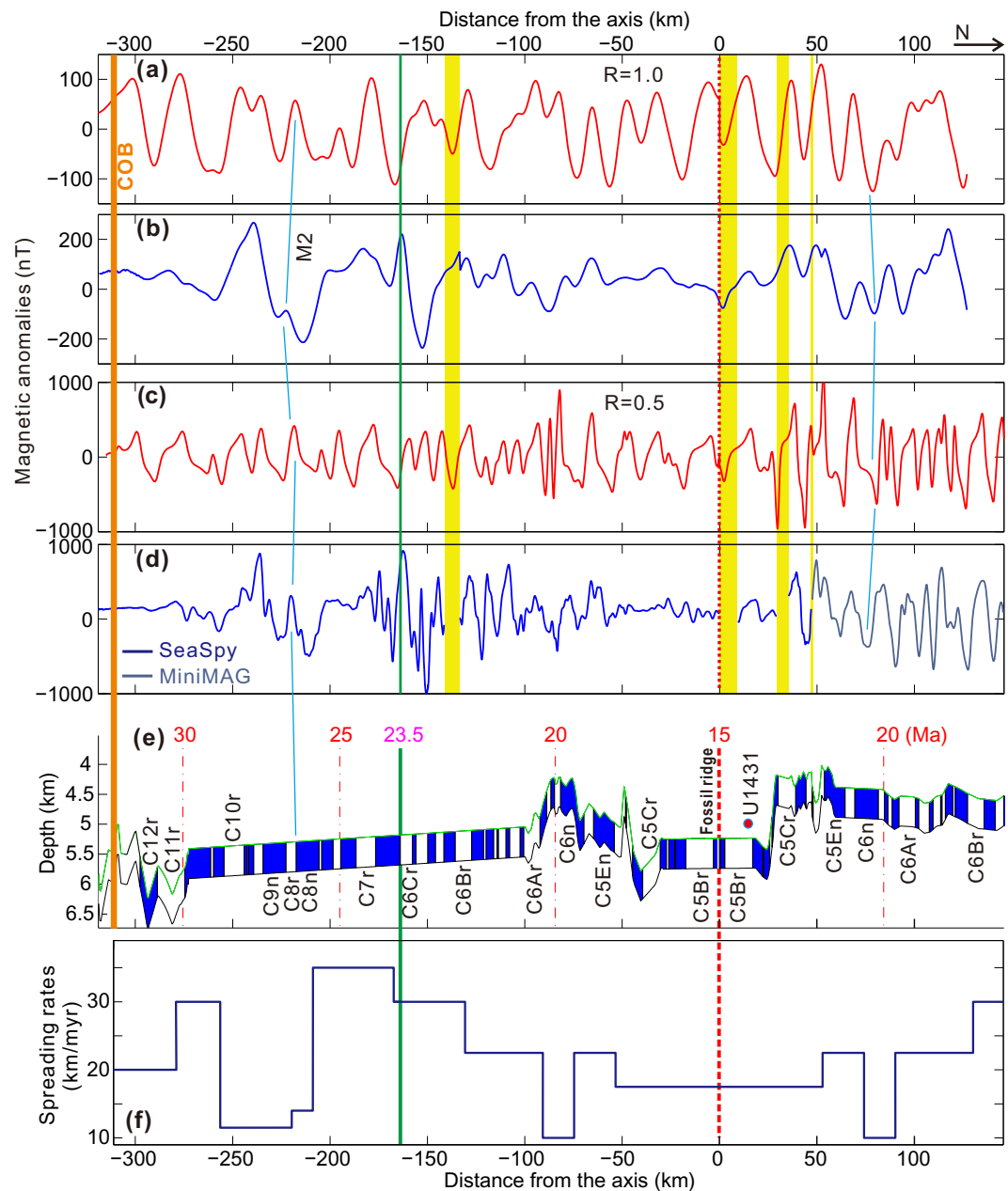


**Figure 11.** Calibration between modeled and observed magnetic anomalies of transect da13. (a) Modeled surface magnetic anomalies; (b) observed surface magnetic anomalies; (c) modeled deep tow magnetic anomalies; (d) observed deep tow magnetic anomalies; (e) the basement magnetization model (blue color indicating normal magnetization). The pink dashed line marks the place of the ridge jump. (f) half spreading rates that were used to construct the model.  $R$  = contamination coefficient; COB = continent-ocean boundary. Vertical yellow bands show data gaps in deep tow magnetic anomalies.

12 shows slightly varying spreading rates from one profile to another. These observations reflect large heterogeneity in the rifting and seafloor spreading kinematics, which can also be evident from regional magnetic anomaly variations in orientations and widths (Figure 8).

#### 4.2.2. Southwest Subbasin

Given the large contrast between the East and Southwest Subbasins in geophysical observations [Li and Song, 2012], some early studies indicated that the Southwest Subbasin might be opened earlier [e.g., Ru and Pigott, 1986; Yao et al., 1994; Li et al., 2007]. This point is in contrast to the commonly held view that the opening of the East and Northwest Subbasins predated, or at least synchronized partly with, that of the

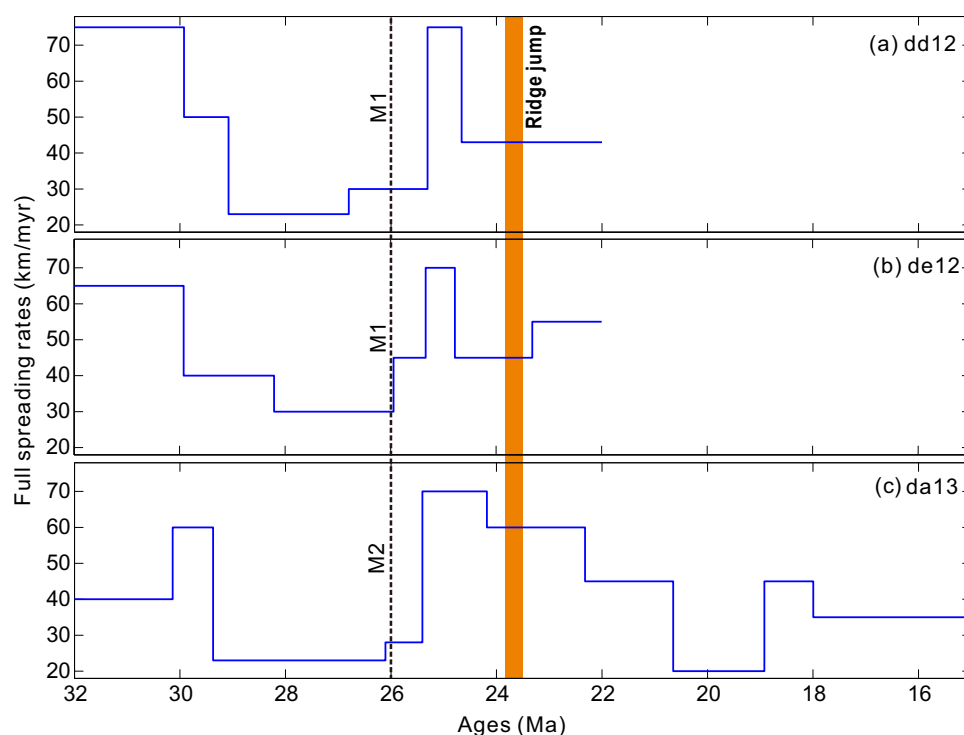


**Figure 12.** Variation with time of full spreading rates estimated from transects dd12, de12, and da13 in the East Subbasin.

Southwest Subbasin [Taylor and Hayes, 1983; Briais *et al.*, 1993; Barckhausen and Roeser, 2004; Barckhausen *et al.*, 2014]. However, the narrow Southwest Subbasin and its relatively weak and irregular magnetic anomalies often pose difficulties in magnetic anomaly calibration [Briais *et al.*, 1993; Song and Li, 2012].

IODP Sites U1433 and U1434 are not located directly on transect dc13, but can be projected to the transect based on regional magnetic anomaly lineation (Figures 13–15). With the age control of these sites and matching of high-resolution deep tow magnetic anomaly, we examine three of the existing age models and present our preference.

Barckhausen *et al.* [2014] suggested that the entire SCS basin stopped spreading at 20.5 Ma and the full spreading rate was 80 km/Myr. With this model, we find that the initial spreading near transect dc13 is about 23.3 Ma; this onset age here is very close to the determined age of the ridge jump that occurred about 400 km further northeast, and we consider this closeness to be unlikely because of the southwestward propagating nature of the rifting/drifting. The modeled crustal age at Site U1433 is 21.45 Ma, which is out of the age range determined from microfossil studies of sediment cores (Table 2). Furthermore, the terminal age of 20.5 Ma of this model appears to be too much larger than the sediment constrained age of ~12 Ma at Site U1434, although we agree that the terminal age should be older than 12 Ma [Expedition 349 Scientists, 2014]. Additionally, the modeled anomalies are not in good match with observed anomalies (Figure 13).

According to the model of Yao *et al.* [1994], opening of the Southwest Subbasin spanned from 35 to 42 Ma. Certainly, with this model, the crustal ages at IODP Sites U1433 and U1434 are expected to be older than 35 Ma, but this apparently is not the case from the drilling records. To check this model, we apply the average spreading rate of 40 km/Myr that is already estimated in the East Subbasin for the age period younger than the ridge jump event (~23.6 Ma). This spreading rate is also close to that taken by Yao *et al.* [1994]. However, the modeled magnetic anomalies cannot match well with observed anomalies (Figure 14).

We now test the model of Briais *et al.* [1993], who estimated that the terminal age is 16 Ma. The magnetic anomalies in the Southwest Subbasin are of higher frequencies and lower amplitudes, and appear spikier,

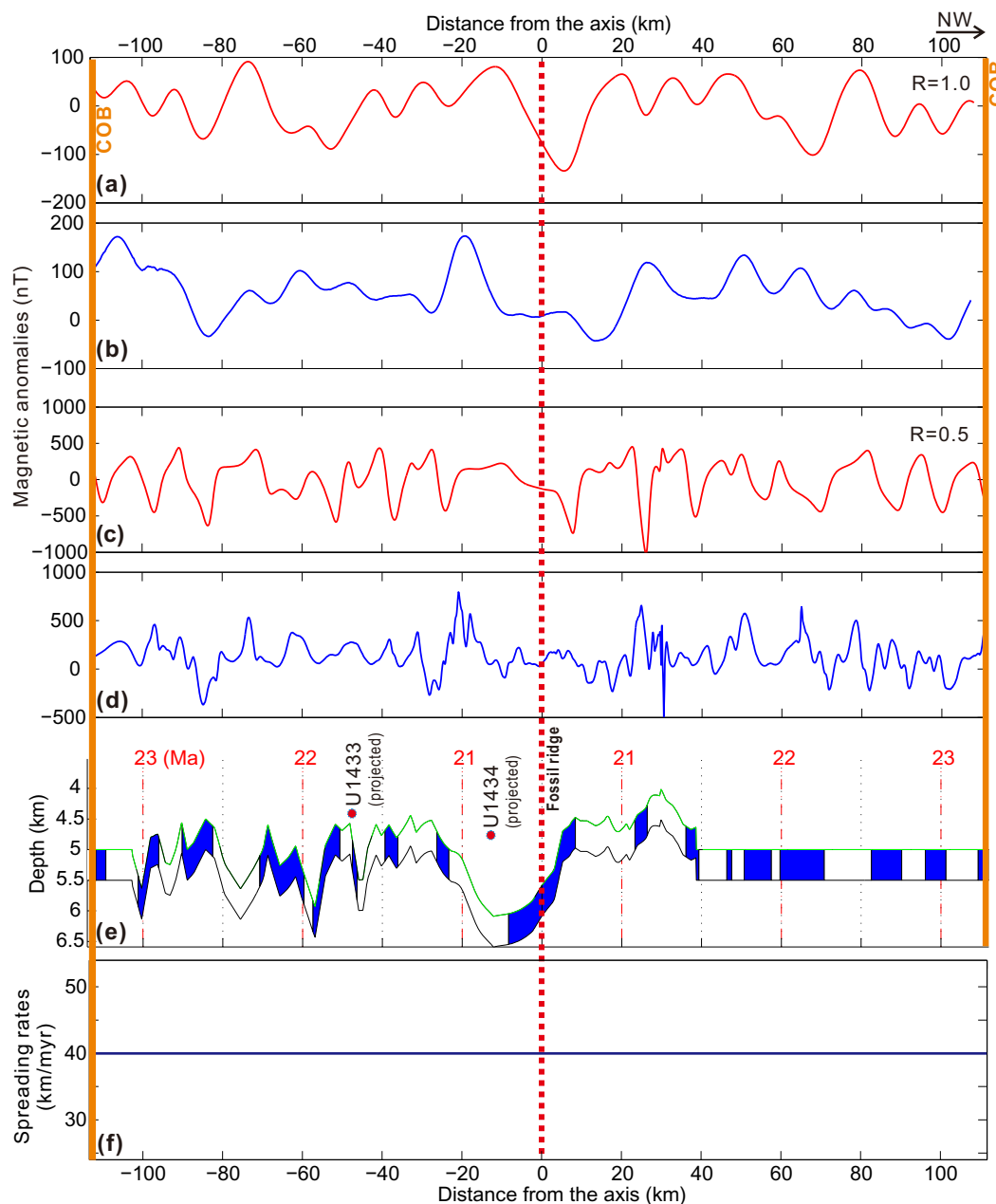


**Figure 13.** Calibration between modeled and observed magnetic anomalies of transect dc13 based on the model of Barckhausen *et al.* [2014]. (a) Modeled surface magnetic anomalies; (b) observed surface magnetic anomalies; (c) modeled deep tow magnetic anomalies; (d) observed deep tow magnetic anomalies; (e) the basement magnetization model (green color indicating normal magnetization); (f) half spreading rates that were used to construct the model.  $R$  = contamination coefficient.

than in the East Subbasin. These complexities in anomalies make it indeed difficult to calibrate. Again, with the average spreading rate of 40 km/Myr, we find from the modeling that this model is conformable to all known constraints, and a good match between modeled and observed anomalies is also observed (Figure 15). We therefore prefer the age model of *Biais et al.* [1993] for the Southwest Subbasin and argue that the terminal age of seafloor spreading here is about 16 Ma [Qiu *et al.*, 2014]. This suggests that the Southwest Subbasin stopped spreading about 1 Ma earlier than the East Subbasin. It is also revealed that the onset of spreading locally at the transect dc13 started at about 21.5 Ma. This is not the earliest onset age of spreading of the Southwest Subbasin, because from the regional magnetic anomaly map (Figure 8), the earliest spreading started further northeast, soon after the ridge jump in the East Subbasin.

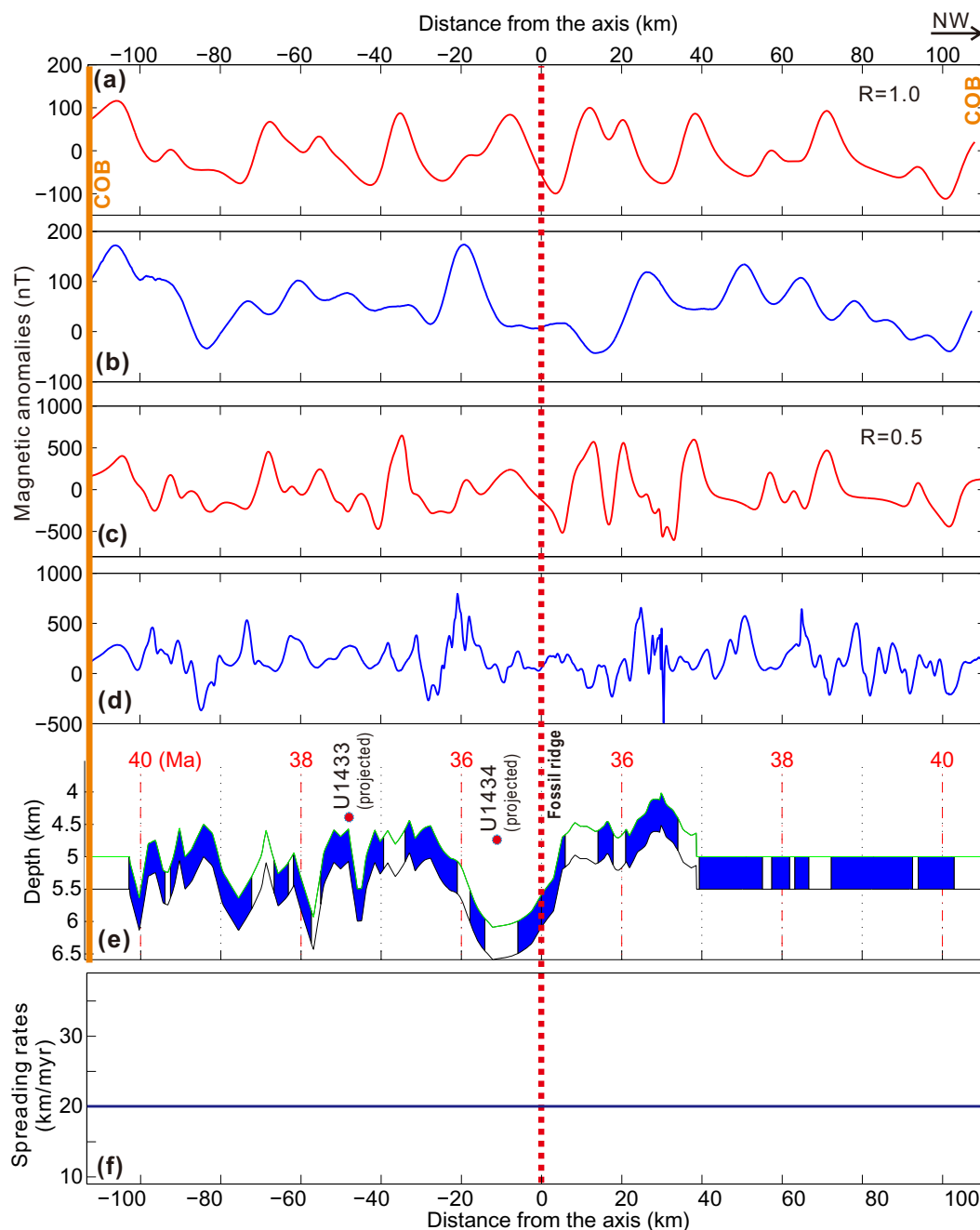
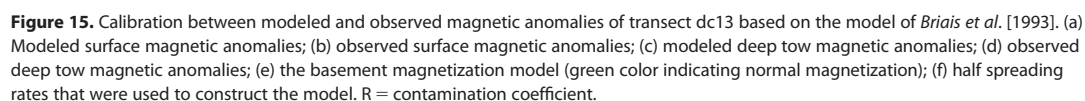


**Figure 14.** Calibration between modeled and observed magnetic anomalies of transect dc13 based on the model of Yao *et al.* [1994]. (a) Modeled surface magnetic anomalies; (b) observed surface magnetic anomalies; (c) modeled deep tow magnetic anomalies; (d) observed deep tow magnetic anomalies; (e) the basement magnetization model (green color indicating normal magnetization); (f) half spreading rates that were used to construct the model.  $R$  = contamination coefficient.

## 5. Inference on Top Magnetic Structures

In our modeling above, we find that computing surface magnetic anomalies with a contamination coefficient  $R = 1.0$  yields acceptable results, but when computing deep tow magnetic anomalies, a smaller  $R = 0.5$  works better (Figures 9, 10, 11, and 15). If we use  $R = 0.5$  for computing surface anomalies, the anomalies will be too smooth, and likewise, using  $R = 1.0$  in modeling deep tow anomalies leads to spiky anomalies. This observation implies that deep tow magnetic anomalies have the advantage and capability of reflecting off-axis intrusions or late-stage lava flows, and/or deeper resources that are magnetized later





IODP Site U1431 penetrated 118.01 m beneath the top of the igneous basement in the East Subbasin, and IODP Site U1433 in the Southwest Subbasin cored 60.81 m into igneous basement (Figures 16 and 17). The

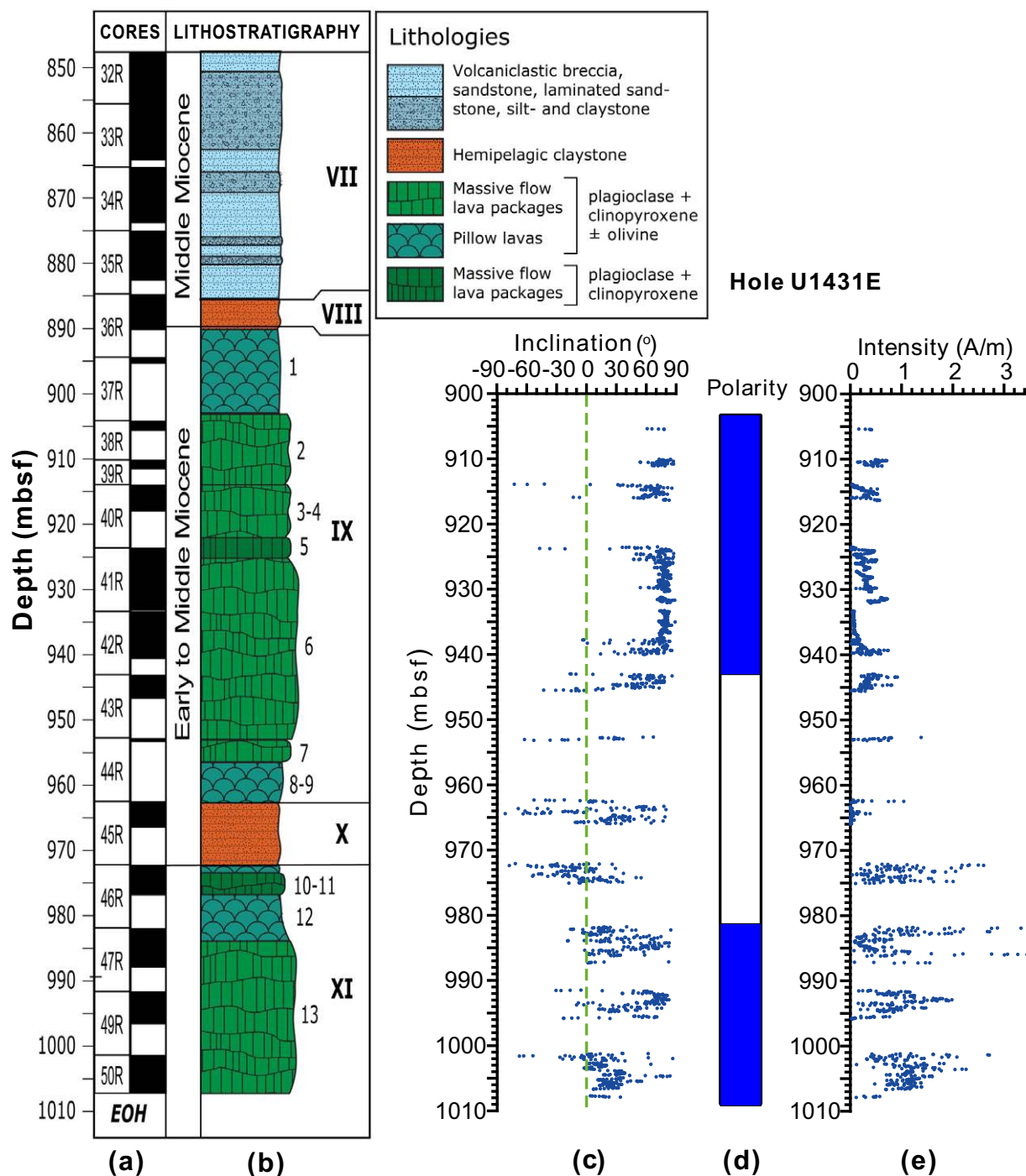


**Figure 16.** Basement lithology and magnetization at Site U1431. (a) Core recovery; (b) lithostratigraphic summary of igneous rock and lithologic features. Arabic numbers indicate igneous lithologic units and Roman numbers indicate lithostratigraphic units; (c) paleomagnetic inclination. The green dashed line indicates the zero inclination line; (d) interpreted magnetostratigraphy. Blue and white indicate normal and reversed polarity, respectively; (e) remanent magnetic intensity. EOH = end of hole.

overall basement recovery at the two sites was reasonably good, at 45.15% [Expedition 349 Scientists, 2014]. From the regional magnetic anomaly map, these two sites sit on positive magnetic anomalies (Figure 8), and based on magnetic parameters in the area and our modeling results, the source magnetizations beneath these anomalies are expected to be transitive from a reversed block to the south to a normal block to the north.

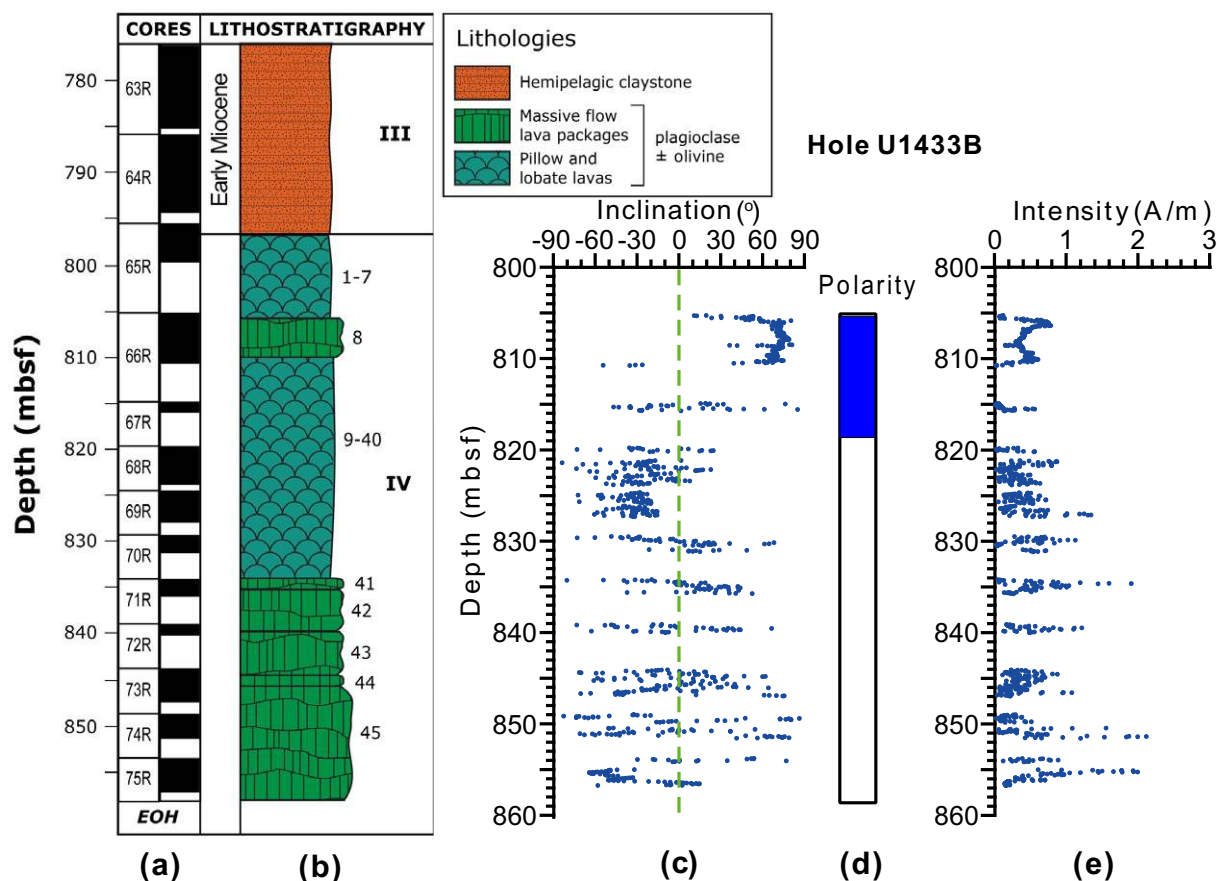


**Figure 17.** Basement lithology and magnetization at Site U1433. (a) Core recovery; (b) lithostratigraphic summary of igneous rock and lithologic features. Arabic numbers indicate igneous lithologic units and Roman numbers indicate lithostratigraphic units; (c) paleomagnetic inclination. The green dashed line indicates the zero inclination line; (d) interpreted magnetostratigraphy. Blue and white indicate normal and reversed polarity, respectively; (e) remanent magnetic intensity. EOH = end of hole.

At both drill sites, shipboard paleomagnetic measurements of basement cores indicate that at least one magnetic reversal event occurred within the very top of the magnetic layer (Figures 16 and 17), in which many lava flow units were identified [Expedition 349 Scientists, 2014]. Site U1431 also shows a ~9 m thick hemipelagic mudstone layer between two basaltic units, further suggesting prolonged magmatic activities during the formation of the oceanic crust. At both sites, the upper intervals of the basaltic layer are normally magnetized based on paleomagnetic inclinations, but downhole transit to reversed polarity. While this could reflect the transitive nature around the possibly inferred magnetic block boundaries causing positive magnetic anomalies, the presence of interflow sediments and magnetic reversals in the top magnetic layer all suggest long periods of magmatic accretion that cause complex magnetization patterns. This observation from these two drill sites confirms our aforementioned inference on basement magnetization from magnetic modeling.

Another factor to consider for the basement magnetization is the remanent magnetization intensity. After 20 mT alternating field demagnetization, the intensities of the basement sections at the two sites all show downhole increasing trends from less than ~1 to 2–2.5 A/m at the bottom, reflecting most likely the decreasing degree of basalt alteration with depth, but the magnetic intensities are all smaller than 3.0 A/m in the recovered intervals (Figures 16 and 17). These observed magnetization intensity values are smaller than that used in our modeling (5.0 A/m), but considering the increasing downhole trend and the much thicker magnetic layer than what we already penetrated through drilling, the overall magnetization of the primary episode of magmatic accretion should be at a similar magnitude to the one we applied in the modeling.

Therefore, based on both modeling and observed magnetic polarity/intensity variations, we can argue that the top 100 m of the igneous basement of the SCS oceanic crust is not the main contributor to observed

magnetic anomalies that are applicable to age dating. The primary magnetic sources are more deeply buried. This is an important inference on the magnetic structure, and could be applicable to other slow to intermediate spreading basins.

Lateral variations in basement magnetization are not directly inverted in this study, but can be easily assessed from the modeling. We find that, with a constant magnetic intensity of 5.0 A/m, the modeled magnetic anomalies are mostly matchable to the observed anomalies in their amplitudes. However, to the north of anomaly M1 and to the south of anomaly M2, the modeled anomalies are much higher within the central basin, even with the consideration of deepened basement carrying the primary magnetization at these areas in the modeling, whereas the observed and modeled anomalies in other segments are in similar scales. We attribute this anomaly difference to lower basement magnetizations in the two areas with the oldest crustal ages, which was also indicated previously from 3-D analytical signal analysis [Li *et al.*, 2008].

Parameters accounting for lateral variation in apparent basement magnetization could include basement depth and composition, alteration of the primary magnetic minerals, long-term changes in the paleomagnetic field intensity, spreading rate and direction, tectonic context, thickness of the magnetic layer, and basaltic alteration. For profiles de12 and dd12, the amplitude of the magnetic anomalies becomes gradually smeared from ~23 to ~31 Ma (Figure 3). However, the modeled magnetic anomalies show rather comparable amplitude throughout the profile (Figures 9 and 10). Therefore, the effects of the basement depth on the magnetic amplitudes can be ruled out since there is not a significant correlation between the amplitude of the magnetic anomalies and the basement depth.

Channell and Lanci [2014] constructed the Oligocene to Miocene (17.5–26.5 Ma) relative paleomagnetic paleointensity (RPI) for the equatorial Pacific, which exhibits a quasi periodicity of ~50 kyr, and typically shows high RPI values at ~23, 24, and ~26 Ma. This pattern seems to be partly consistent with the observed deep-tow anomalies that also show relatively high amplitudes around these ages (Figures 9 and 10).

Observed magnetic anomalies can reflect changes in the magnetic assemblage in terms of the concentration, domain state, and the degree of low-temperature oxidation. For magnetic particles with grain size larger than the superparamagnetic size, the remanence magnetization will be inversely related to grain size [Dunlop and Özdemir, 1997; Liu *et al.*, 2012]. Low-temperature oxidation can greatly attenuate the anomaly intensity by the maghemitization processes that transform (titano)magnetite to (titano)maghemite [Zhou *et al.*, 2001], and it is reasonable to expect that magnetic particles in older rocks with higher degrees of low-temperature oxidation and alteration have lower magnetic susceptibility [e.g., Wang *et al.*, 2005]. While this could explain the low magnetic anomalies in the two areas of the central basin to the north of anomaly M1 and to the south of anomaly M2, the sharp boundaries of M1 and M2 seem to be at odds with this suggestion.

In summary, compositional variations in basement mineralogy and geochemistry appear to be the primary and most plausible explanation for observed variations in apparent magnetization, whereas spreading rates and relative paleomagnetic paleointensity could have also contributed to the complexity. From magnetic anomalies, it seems that basement rocks are less mafic and lower in magnetic susceptibility in the entire narrow Southwest Subbasin and in areas adjacent to the continents in the East Subbasin, probably indicating more continental influences on their magma sources [Pautot *et al.*, 1986; Li *et al.*, 2008].

## 6. Conclusions

Two comprehensive magnetic surveys deploying five sets of different instruments (deep-towed proton precession and three-axis magnetoresistor magnetometers, surface-towed proton precession magnetic gradiometer and three-axis fluxgate magnetometer, and seafloor geomagnetic base station) with the newly built R/V Haiyang 6 acquired 1220 km of deep tow magnetic anomalies for the first time offshore coastal China. These high-resolution and large-amplitude magnetic data along four carefully selected transects, together with discoveries from International Ocean Discovery Program (IODP) Expedition 349 finished in 2014, provide a unique opportunity to reassess current opening models of the SCS.

The earliest opening of the East Subbasin of the SCS started in the northeastern part of the basin around 33 Ma based on the age of an unconformity at IODP Site U1435, but the onset of seafloor spreading near IODP Sites U1432 and U1435 occurred around 31.5 Ma based on our deep tow magnetic anomaly modeling. This



time difference indicates discontinuous initial spreading along the present-day continent-ocean boundary (COB). The terminal age of seafloor spreading in the East Subbasin is estimated at  $\sim 15$  Ma, and the terminal age is  $\sim 16$  Ma in the Southwest Subbasin.

Modeling results of three deep tow transects support that a ridge jump occurred around 23.6 Ma, though varying slightly in timing from place to place. The distance of this southward jump in spreading center is about 20 km. It accounts primarily for the asymmetry in basin width across the relict spreading center. We suspect that the ridge jump that occurred around 23.6 Ma in the East Subbasin also represents the age of initial onset of opening of the Southwest Subbasin. These modeled ages fit well with age constraints based on microfossils in recovered cores from IODP Expedition 349. Overall, our age model is closer to or more consistent with the early models of *Taylor and Hayes* [1980, 1983] and *Briaïs et al.* [1993] than to other proposed models.

Our modeling suggests that the full spreading rate in the East Subbasin varies from  $\sim 20$  to  $\sim 80$  km/Myr, putting the SCS into a low to intermediate spreading basin. Spreading started at a relatively high rate and lasted for about 3 Myr, and then dropped to about  $\sim 25$  km/Myr on average from  $\sim 29$  to  $\sim 26$  Ma before the occurrence of magnetic anomalies M1 and M2. From M1 and M2 to the ridge jump, the spreading rate maintained a high rate of about 70 km/Myr, and afterward the spreading rate variably decreased from  $\sim 50$  to  $\sim 35$  km/Myr at the end of seafloor spreading. Our calibrated spreading rates are quite opposite to those proposed by *Barckhausen et al.* [2014], who suggested faster spreading rates that even increased after the ridge jump to 72 km/Myr in the East Subbasin.

Both deep tow magnetic modeling and measured magnetic polarities from IODP Expedition 349 cores suggest late-stage lava flows and/or deeper magnetic sources that were magnetized later in a different polarity from that of the primary basaltic layer emplaced during the main phase of crustal accretion. These geological processes are revealed by measured magnetic anomalies, but more so with deep towed than surface-towed anomalies, implying that deep tow magnetic anomalies are more sensitive to basement complexities than surface anomalies as the deep tow measurements are made closer to the magnetic sources. We observe that the primary contributor to apparent magnetization variations is basement mineralogy and geochemistry, but locally spreading rates and relative paleomagnetic paleointensity may also play secondary roles.

#### Acknowledgment

This paper benefited greatly from the thorough and constructive reviews by Roi Granot and an anonymous reviewer. This research is funded by National Science Foundation of China (grant 91028007, grant 91428309), Program for New Century Excellent Talents in University, and Research Fund for the Doctoral Program of Higher Education of China (grant 20100072110036). This research also used samples and/or data provided by the International Ocean Discovery Program (IODP). We thank the officers, technician, engineers, and crew members of R/V Haiyang 6 and D/V JOIDES Resolution for their critical contributions. Data mapping is supported by GMT [Wessel and Smith, 1995]. Faguang He, Xiaojuan Qu, Shengxuan Liu, Xiuyun Cui, and Xiangyu Zhang of GMGS and Jiansheng Wu, Jun Chen, Xinbing Zhang, and Tingting Wang of Tongji University also participated in the deep tow project. Data related to IODP Expedition 349 will be available for downloading from the IODP website (www.iodp.org) after the moratorium period, which will end on 30 March 2015. Original deep tow magnetic data used in this study could be available upon request to the PIs of the deep tow project (C.-F. Li, J. Lin, Z. Sun, and X. Xu), who make the collective decision.

#### References

- Barckhausen, U., and H. A. Roeser (2004), Seafloor spreading anomalies in the South China Sea revisited, in *Continent-Ocean Interactions Within East Asian Marginal Seas*, *Geophys. Monogr. Ser.*, vol. 149, edited by P. Clift et al., pp. 121–125, AGU, Washington, D. C.
- Barckhausen, U., M. Bagge, and D. S. Wilson (2013), Seafloor spreading anomalies and crustal ages of the Clarion-Clipperton Zone, *Mar. Geophys. Res.*, **34**, 79–88, doi:10.1007/s11001-013-9184-6.
- Barckhausen, U., M. Engels, D. Franke, S. Ladage, and M. Pubellier (2014), Evolution of the South China Sea: Revised ages for breakup and seafloor spreading, *Mar. Pet. Geol.*, 599–611, doi:10.1016/j.marpetgeo.2014.02.022.
- Becker, J. J., et al. (2009), Global bathymetry and elevation data at 30 arc seconds resolution: SRTM30\_PLUS, *Mar. Geod.*, **32**, 355–371.
- Braitenberg, C., S. Wienecke, and Y. Wang (2006), Basement structures from satellite-derived gravity field: South China Sea ridge, *J. Geophys. Res.*, **111**, B05407, doi:10.1029/2005JB003938.
- Briaïs, A., P. Patriat, and P. Tapponnier (1993), Updated interpretation of magnetic anomalies and seafloor spreading stages in the South China Sea: Implications for the Tertiary tectonics of Southeast Asia, *J. Geophys. Res.*, **98**, 6299–6328.
- Cande, S. V., and D. V. Kent (1995), Revised calibration of the geomagnetic polarity timescale for the late Cretaceous and Cenozoic, *J. Geophys. Res.*, **100**, 6093–6095.
- Channell, J. E. T., and L. Lanci (2014), Oligocene-Miocene relative (geomagnetic) paleointensity correlated from the equatorial Pacific (IODP Site U1334 and ODP Site 1218) to the South Atlantic (ODP Site 1090), *Earth Planet. Sci. Lett.*, **387**, 77–88.
- Cordell, L. (1985), Techniques, applications, and problems of analytical continuation of New Mexico aeromagnetic data between arbitrary surfaces of very high relief [abstract], in *Proceedings of the International Meeting on Potential Fields in Rugged Topography*, *Bull. 7*, pp. 96–99, Inst. of Geophys., Univ. of Lausanne, Lausanne, Switzerland.
- Cordell, L., J. D. Phillips, and R. H. Godson (1993), USGS potential-field geophysical software for PC and compatible microcomputers, *Leading Edge*, **12**, 290.
- Ding, W., D. Franke, J. Li, and S. Steuer (2013), Seismic stratigraphy and tectonic structure from a composite multi-channel seismic profile across the entire Dangerous Grounds, South China Sea, *Tectonophysics*, **582**, 162–176.
- Dunlop, D. J., and Ö. Özdemir (1997), *Rock Magnetism: Fundamentals and Frontiers*, 596 pp., Cambridge Univ. Press, Cambridge, U. K.
- Expedition 349 Scientists (2014), Opening of the South China Sea and its implications for southeast Asian tectonics, climates, and deep mantle processes since the late Mesozoic, *Int. Ocean Discovery Program Prelim. Rep.*, **349**, 1–109, doi:10.14379/iodp.pr.349.2014.
- Franke, D., U. Barckhausen, N. Baristean, M. Engels, S. Ladage, R. Lutz, J. Montano, N. Pellejera, E. G. Ramos, and M. Schnabel (2011), The continent-ocean transition at the southeastern margin of the South China Sea, *Mar. Pet. Geol.*, **28**(6), 1187–1204.
- Gee, J., S. Webb, J. Ridgway, H. Staudigel, and M. Zumberge (2001), A deep tow magnetic survey of Middle Valley, Juan de Fuca Ridge, *Geochem. Geophys. Geosyst.*, **2**(11), 1059, doi:10.1029/2001GC000170.

- Gee, J. S., S. C. Cande, J. A. Hildebrand, K. Donnelly, and R. L. Parker (2000), Geomagnetic intensity variations over the past 780 kyr obtained from near-seafloor magnetic anomalies, *Nature*, **408**, 827–832.
- Gradstein, F., J. Ogg, and A. Smith (Coords) (2004), *A Geologic Time Scale 2004*, pp. 1–610, Cambridge Univ. Press, Cambridge, U. K.
- Gradstein, F. M., J. G. Ogg, M. D. Schmitz, and G. M. Ogg (Coords) (2012), *The Geologic Time Scale 2012*, 2 volumes plus chart, 1176 pp., Elsevier, Boston, Mass.
- Granot, R., J. Dymment, and Y. Gallet (2012), Geomagnetic field variability during the Cretaceous Normal Superchron, *Nat. Geosci.*, **5**, 220–223.
- Greenewalt, D., and P. T. Taylor (1978), Near-bottom magnetic measurements between the FAMOUS area and DSDP sites 332 and 333, *Geol. Soc. Am. Bull.*, **89**, 571–576.
- Hayes, D. E. and S. S. Nissen (2005), The South China Sea margins: Implications for rifting contrasts, *Earth Planet. Sci. Lett.*, **237**(3–4), 601–616.
- Hsu, S.-K., Y. Yeh, W.-B. Doo, and C.-H. Tsai (2004), New bathymetry and magnetic lineations identifications in the northernmost South China Sea and their tectonic implications, *Mar. Geophys. Res.*, **25**(1–2), 29–44.
- Hussenoeder, S. A., M. A. Tivey, H. Schouten and R. C. Searle (1996), Near-bottom magnetic survey of the Mid-Atlantic Ridge axis, 24–2440N: Implications for crustal accretion at slow spreading ridges, *J. Geophys. Res.*, **101**, 22,051–22,069.
- International Association of Geomagnetism and Aeronomy (IAGA), Working Group V-MOD (2010), International geomagnetic reference field: The eleventh generation, *Geophys. J. Int.*, **183**, 1216–1230.
- Ishihara, T., and K. Kisimoto (1996), Magnetic anomaly map of East Asia, scale 1:4,000,000 [CD-ROM], Geol. Surv. of Jpn. and Coord. Comm. for Costal and Offshore Geosci. Programs in East and Southeast Asia, Tokyo, Japan.
- Kidd, R. G. W. (1977), The nature and shape of the sources of marine magnetic anomalies, *Earth Planet. Sci. Lett.*, **33**(3), 310–320.
- Li, C.-F., and T. Song (2012), Magnetic recording of the Cenozoic oceanic crustal accretion and evolution of the South China Sea Basin, *Chin. Sci. Bull.*, **57**(24), 3165–3181.
- Li, C.-F., Z. Zhou, J. Li, H. Hu, and J. Geng (2007), Structures of the northeasternmost South China Sea continental margin and ocean basin: Geophysical constraints and tectonic implications, *Mar. Geophys. Res.*, **28**, 59–79.
- Li, C.-F., Z. Zhou, J. Li, B. Chen, and J. Geng (2008), Magnetic zoning and seismic structure of the South China Sea ocean basin, *Mar. Geophys. Res.*, **29**(4), 223–238.
- Li, C.-F., et al. (2009), Opening of the South China Sea and its implications for Southeast Asian tectonics since the late Mesozoic—Introduction to IODP Proposal 735-Full [in Chinese], *Adv. Earth Sci.*, **24**(12), 1339–1351.
- Li, C.-F., X. Shi, Z. Zhou, J. Li, J. Geng, and B. Chen (2010), Depths to the magnetic layer bottom in the South China Sea area and their tectonic implications, *Geophys. J. Int.*, **182**(3), 1229–1247.
- Li, C.-F., J. Lin, and D. K. Kulhanek (2013), South China Sea tectonics: Opening of the South China Sea and its implications for southeast Asian tectonics, climates, and deep mantle processes since the late Mesozoic, *Int. Ocean Discovery Program Sci. Prospectus*, **349**, 1–111, doi:10.2204/iodp.sp.349.2013.
- Li, Q., Z. Jian, and B. Li (2004), Oligocene-Miocene planktonic foraminifer biostratigraphy, Site 1148, northern South China Sea, in *Proceedings of the Ocean Drilling Program, Scientific Results*, vol. 184, edited by W. L. Prell et al., pp. 1–26, Ocean Drill. Program, College Station, Tex.
- Lin J., X. Xu, C.-F. Li, Z. Sun, J. Zhu, Z. Zhou, and N. Qiu (2013), First high-resolution near seafloor survey of magnetic anomalies of the South China Sea, Abstract #OS23E-01 presented at AGU Fall Meeting 2013, AGU, San Francisco, Calif.
- Liu, Q. S., A. P. Roberts, J. C. Larrasoana, S. K. Banerjee, Y. Guyodo, L. Tauxe, and F. Oldfield (2012), Environmental magnetism: Principles and applications, *Rev. Geophys.*, **50**, RG4002, doi:10.1029/2012RG000393.
- Macdonald K. C., K. Kastens, F. N. Spiess, and S. P. Miller (1979), Deep tow studies of the Tamayo Transform Fault, *Mar. Geophys. Res.*, **4**, 37–70.
- McIntosh, K., H. van Avendonk, L. Lavier, W. R. Lester, D. Eakin, F. Wu, C.-S. Liu, and C.-S. Lee (2013), Inversion of a hyper-extended rifted margin in the southern Central Range of Taiwan, *Geology*, **41**, 871–874.
- Mendel, V., M. Munschy, and D. Sauter (2005), MODMAG, a MATLAB program to model marine magnetic anomalies, *Comput. Geosci.*, **31**(5), 589–597.
- Müller, R. D., M. Sdrolias, C. Gaina, and W. R. Roest (2008), Age, spreading rates, and spreading asymmetry of the world's ocean crust, *Geochem. Geophys. Geosyst.*, **9**, Q04006, doi:10.1029/2007GC001743.
- Nguyen, N. T., S.-M. Lee, and C. Q. Bui (2004), Satellite gravity anomalies and their correlation with the major tectonic features in the South China Sea, *Gondwana Res.*, **7**(2), 407–424.
- Pautot, G., C. Rangin, A. Briaes, P. Tapponnier, P. Beuzart, G. Lericolais, X. Mathieu, J. Wu, S. Han, H. Li, Y. Lu, and J. Zhao (1986), Spreading direction in the central South China Sea, *Nature*, **321**(6066), 150–154.
- Perram, L. J., K. C. Macdonald, and S. P. Miller (1990), Deep-tow magnetics near 20 Ma on the East Pacific Rise: A study of short wavelength anomalies at a very fast spreading center, *Mar. Geophys. Res.*, **12**, 235–245.
- Phillips, J. D. (1997), Potential-Field Geophysical Software for the PC, version 2.2, open file report, 97–725. U.S. Department of the Interior, U.S. Geol. Surv. Denver, USA. [Available at <http://pubs.usgs.gov/of/1997/ofr-97-0725/>]
- Pouliquen, G., Y. Gallet, J. Dymment, P. Patriat, and C. Tamura (2001), A geomagnetic record over the last 3.5 million years from deep-tow magnetic anomaly profiles across the Central Indian Ridge, *J. Geophys. Res.*, **6**, 10,941–10,960.
- Qiu, N., Z. Sun, J. Lin, C.-F. Li, and X. Xu (2014), Geomagnetic polarity reversal model of deep-tow magnetic survey in the Southwest Subbasin of South China Sea ridge, Abstract presented at 2014 AGU Fall Meeting, GP23A-3658, AGU, San Francisco, Calif.
- Ru, K., and J. D. Pigott (1986), Episodic rifting and subsidence in the South China Sea, *AAPG Bull.*, **70**, 1136–1155.
- Sager, W. W., C. J. Weiss, M. A. Tivey, and H. P. Johnson (1998), Geomagnetic polarity reversal model of deep-tow profiles from the Pacific Jurassic Quiet Zone, *J. Geophys. Res.*, **103**, 5269–5286.
- Sandwell, D., E. Garcia, K. Soofi, P. Wessel, M. Chandler, and W. H. F. Smith (2013), Toward 1-mGal accuracy in global marine gravity from CryoSat-2, Envisat, and Jason-1, *Leading Edge*, **32**(8), 892–899.
- Sandwell, D. T., and W. H. F. Smith (2009), Global marine gravity from retracked Geosat and ERS-1 altimetry: Ridge segmentation versus spreading rate, *J. Geophys. Res.*, **114**, B01411, doi:10.1029/2008JB006008.
- Song, T., and C.-F. Li (2012), The opening ages and mode of the South China Sea estimated from high-density magnetic tracks [in Chinese], *Prog. Geophys.*, **27**(4), 1432–1442.
- Talwani, M., and J. R. Heirtzler (1964), Computation of magnetic anomalies caused by two-dimensional structures of arbitrary shapes, in *Computers in the Mineral Industries*, *Geol. Sci.*, vol. 9, pp. 464–479, Stanford Univ. Publ., Calif, USA.

- Taylor, B., and D. E. Hayes (1980), The tectonic evolution of the South China Basin, in *The Tectonic and Geologic Evolution of Southeast Asian Seas and Islands*, *Geophys. Monogr. Ser.*, vol. 23, edited by D. E. Hayes, pp. 89–104, AGU, Washington, D. C.
- Taylor, B., and D. E. Hayes (1983), Origin and history of the South China Sea Basin, in *The Tectonic and Geologic Evolution of Southeast Asian Seas and Islands (Pt. 2)*, *Geophys. Monogr. Ser.*, vol. 27, edited by D. E. Hayes, pp. 23–56, AGU, Washington, D. C.
- Tisseau, J., and P. Patriat (1981), Identification des anomalies magnétiques sur les dorsales à faible taux d'expansion: Méthode des taux fictifs, *Earth Planet. Sci. Lett.*, 52, 381–396.
- Tivey, M. A. (1996), Vertical magnetic structure of ocean crust determined from near-bottom magnetic field measurements, *J. Geophys. Res.*, 101, 20,275–20,296.
- Tivey, M. A., and H. P. Johnson (2002), Crustal magnetization reveals subsurface structure of Juan de Fuca, *Geology*, 30(11), 979–982.
- Tominaga, M., W. W. Sager, M. A. Tivey, and S.-M. Lee (2008), Deep-tow magnetic anomaly study of the Pacific Jurassic Quiet Zone and implications for the geomagnetic polarity reversal timescale and geomagnetic field behavior, *J. Geophys. Res.*, 113, B07110, doi:10.1029/2007JB005527.
- Wang, D., R. Van der Voo, and D. R. Peacor (2005), Low-temperature alteration and magnetic changes of variably altered pillow basalts, *Geophys. J. Int.*, 164(1), 25–35.
- Wang, P., et al. (2000), *Proceedings of Ocean Drilling Program, Initial Report*, vol. 184, Ocean Drill. Program, College Station, Tex.
- Wessel, P., and W. H. F. Smith (1995), New version of the Generic Mapping Tools (GMT) version 3.0 released, *Eos Trans. AGU*, 76, 329.
- Whitmarsh, R. B., P. R. Miles, J.-C. Sibuet, and V. Louvel (1996), Geological and geophysical implications of deep-tow magnetometer observations near sites 897, 898, 899, 900, and 901 on the west Iberia continental margin, in *Proceedings of the Ocean Drilling Program, Scientific Results*, vol. 149, edited by R. B. Whitmarsh et al., pp. 665–674, Ocean Drill. Program, College Station, Tex.
- Yamamoto, M., N. Seama, and N. Isezaki (2005), Geomagnetic paleointensity over 1.2 Ma from deep-tow vector magnetic data across the East Pacific Rise, *Earth Planets Space*, 57, 465–470.
- Yao, B. (1995), Characteristics and tectonic significance of the Zhongnan-Liyue Fault [in Chinese], *Memo. 7*, pp. 1–14, *Geol. Res. of the South China Sea*, Guangzhou, China.
- Yao, B., W. Zeng, Y. Chen, X. Zhang, D. E. Hayes, J. Diebold, P. Buhl, and S. Spangler (1994), *The Geological Memoir of South China Sea Surveyed Jointly by China and USA* [in Chinese], pp. 1–204, China Univ. of Geosci. Press, Wuhan, China.
- Zhou, W., R. Van der Voo, D. R. Peacor, D. Wand, and Y. Zhang (2001), Low-temperature oxidation in MORB of titanomagnetite to titanomaghemite: A gradual process with implications for marine magnetic anomaly amplitudes, *J. Geophys. Res.*, 106, 6409–6421.
- Zhu, J., J. Lin, Y. Chen, C. Tao, C. German, D. Yoerger, and M. Tivey (2010), A reduced crustal magnetization zone near the first observed active hydrothermal vent field on the Southwest Indian Ridge, *Geophys. Res. Lett.*, 37, L18303, doi:10.1029/2010GL043542.